Marine Geology 416 (2019) 105987

Contents lists available at ScienceDirect

Marine Geology

journal homepage: www.elsevier.com/locate/margo

Investigating ENSO and WPWP modulated typhoon variability in the South China Sea during the mid–late Holocene using sedimentological evidence from southeastern Hainan Island, China

Liang Zhou[a], Yang Yang[a], Zhanghua Wang[a,b], Jianjun Jia[a], Longjiang Mao[c], Zhanhai Li[a], Xin Fang[d], Shu Gao[a,*]

[a] State Key Laboratory of Estuarine and Coastal Research, ECNU, Shanghai 200062, China
[b] Institute of Urban and Regional Development Research, ECNU, Shanghai 200062, China
[c] School of Marine Sciences, Nanjing University of Information Sciences & Technology, Nanjing 210044, China
[d] Second Institute of Oceanography, Ministry of Natural Resources, Hangzhou 310012, China

ARTICLE INFO

Editor: Edward Anthony

Keywords:
Typhoons
Lagoonal sequence
South China Sea
Western North Pacific
Mid-to-late Holocene
ENSO
WPWP

ABSTRACT

The link between tropical cyclone (TC) activity in the South China Sea (SCS) and global climate change is commonly debated and there is a clear need for long-term geological records of TC activity if we are to clarify this connection. Multi-millennial, high-resolution paleo-storm records from the SCS are rare in the region and this causes difficulties for those exploring potential climate drivers of TC variability over centennial to millennial timescales and reduces our ability to fully assess the risks associated with future TC activity. This paper presents an age-constrained, mud-dominated sedimentary sequence from a coastal lagoon on Hainan Island, China. Multiproxy analyses incorporating chronological, lithological, sedimentological, and geochemical evidence were used to infer storm deposits preserved within the sequence and to reconstruct a time series of storm activity in the SCS during the mid-to-late Holocene. This long sedimentary record shows that TCs were highly active over the periods 5500 to 3500 and 1700 to 0 cal yrs. BP, and these periods contrast with a relatively quiet period 3500–1700 cal yrs. BP. An apparent inverse correlation between TC reconstructions from the SCS and those from the Korean Peninsula and Japan implies an oscillating pattern across the SCS and western North Pacific (WNP) over centennial to millennial timescales. A comparison between the sedimentary and paleoclimatic records implies that the El Niño–Southern Oscillation was not the only mechanism responsible for typhoon variability over the past 7500 cal yrs. BP, suggesting that other factors such as the thermal state of the western Pacific warm pool likely also had a strong influence on both SCS and WNP TC variability.

1. Introduction

The inhabitants of coastal areas of South China Sea (SCS) and the Western North Pacific (WNP) are experiencing increasingly frequent and intense typhoons that are causing significant societal and economic problems, as was demonstrated by the catastrophic impact of Typhoon Haiyan on the Philippines in 2013 (Soria et al., 2016). Such disastrous events have fueled the debate over whether the recent increases in the intensity and frequency of typhoon activity should be attributed to the warming of the global oceans and climate (e.g. Emanuel, 2005; Gaertner et al., 2007; Stowasser et al., 2007; Mann et al., 2009; Knutson et al., 2010; Mendelsohn et al., 2012; Nissen et al., 2014). The major problem with this debate is that we know little about how the complex mechanisms that drive the generation, track shift, and evolution of typhoons in this WNP and SCS have been altered by the climate (Woodruff et al., 2009). This is partly because accurate records of TC activity begin in 1945 CE, which is too short an interval to assess any changes occurring over multi-centennial to millennial time scales. Thus, researchers are increasingly using geological evidence to extend the length of typhoon activity records beyond the instrumental period and thereby develop a better understanding of the possible linkage between future climate change and increasing storm intensity and frequency (e.g. Liu and Fearn, 1993; Nott, 2004; Woodruff et al., 2009; Reed et al., 2015; Toomey et al., 2016; Lau et al., 2016).

This field of paleotempestology (Nott, 2004; Liu, 2007; Hippensteel, 2010), was developed to enable millennial or longer-period studies of storm activity (Liu and Fearn, 1993; Donnelly et al., 2001, 2004; Liu et al., 2001; Woodruff et al., 2009; Toomey et al., 2016) using

* Corresponding author.
E-mail address: sgao@sklec.ecnu.edu.cn (S. Gao).

https://doi.org/10.1016/j.margeo.2019.105987
Received 5 March 2019; Received in revised form 12 July 2019; Accepted 12 July 2019
Available online 18 July 2019

geological records (Nott, 2004; Liu, 2007; Toomey et al., 2016). Geological proxies of storm activity include storm-induced beach ridges and cheniers (Hayne and Chappell, 2001; Nott and Hayne, 2001), storm-related deposits in estuarine–deltaic environments, paleontological analysis, organic geochemical signatures from coastal lakes (Das et al., 2013), and $\delta^{18}O$ records from speleothems (Malmquist, 1997; Frappier et al., 2007). The storm-induced coarse-grained deposits preserved within back-barrier lagoonal environments have been recognized as a particularly effective proxy and widely used to extend records of TC landfalls over the southern and eastern United States (Liu and Fearn, 1993; Donnelly et al., 2004; Donnelly and Woodruff, 2007; Boldt et al., 2010; Brandon et al., 2013), the Mediterranean (e.g. Sabatier et al., 2008, 2010, 2012; Degeai et al., 2015; Raji et al., 2015; Dezileau et al., 2016), the Central Pacific (Toomey et al., 2013; Lau et al., 2016), Western Australia (Nott, 2011), East Asia (Woodruff et al., 2009), and the SCS (e.g. Yu et al., 2009a).

Some studies based on meteorological data have shown that El Niño-Southern Oscillation (ENSO) strongly affects TC activity in the SCS and WNP (e.g. Chan, 1985, 2005; Lander, 1994; Wang and Chan, 2002; Camargo et al., 2007; Cao et al., 2014). However, its influence is different within the two areas. The overall number of TCs does not differ significantly between El Niño and La Niña years (Wang and Chan, 2002). However, during La Niña (El Niño) years, TCs appear more (less) frequently, form farther westward (eastward), and are more likely to curve backward towards the Northern SCS (Southern China; Wang and Chan, 2002).

Several studies of long-term patterns have suggested that storm activity across the WNP basin has varied over centennial to millennial time scales over the past 5000 years (e.g. Woodruff et al., 2009; Chen et al., 2012; Katsuki et al., 2016; Yang et al., 2017b). Centennial-to millennial-scale typhoon reconstructions for southwestern Japan and southern Korea (northeastern WNP) indicate that ENSO has likely played a key role in governing typhoon variability during the mid-to-late Holocene (e.g. Woodruff et al., 2009; Yang et al., 2017b). However, other climatic factors (e.g. the East Asia summer monsoon (EASM) pattern, the expansion of the WPWP) are also thought to have limited El Niño-like variability during the mid-to-late Holocene (Chen et al., 2012; Katsuki et al., 2016; Yang et al., 2017b), possibly restraining TC activity in the SCS. In comparison with the northeastern WNP, there is a lack of continuous, high-resolution millennial-scale storm records from the SCS (e.g. Yu et al., 2009a; Zhou et al., 2017). Historical documents that record typhoon landfalls from Guangdong and Hainan Provinces in Southern China extend back 1000 years, and complete records for typhoon strikes to the region are likely to be reliable back to only 1600 CE (Chen, 1995; Liu et al., 2001). Geological reconstructions of storm frequency for the SCS are restricted to a few dated reef blocks along reef flats on Nansha and other nearby islands (Yu et al., 2004;Yu et al., 2009a). Radiocarbon and U-series dating of these reef blocks have yielded calibrated ages between 78 and 1640 yrs. BP (Zhu et al., 1991; Yu et al., 2004). These low-resolution records limit our ability to characterize higher-frequency patterns in the SCS and storm activity across the whole basin.

Hainan Island, south China (Fig. 1a), is one of the areas in the WNP that is most frequently and seriously affected by storms (Goh and Chan, 2010; Yap et al., 2015). Reliable instrumental data for this area began in 1949 CE (http://www.typhoon.org.cn/). According to the best track dataset for the WNP, a total of 87 TCs crossed Hainan Island between 1964 and 2013, with an average recurrence rate of 1.7 per year and a maximum of 5 events in 1971 (Liang et al., 2015). Prior to the best track dataset, the documentary archives of paleostorm information can be traced back to the Song Dynasty (960–1279 CE) and the Yuan Dynasty (1271–1368 CE), but detailed accounts of storm events are available for only the past 500 years (Chen, 1995; Wen, 2007).

In addition, the historical seismic records show that earthquakes with a magnitude > 7.0 are rare in the oceanic area close to Hainan Island (Mak and Chan, 2007). Recent studies (Li et al., 2016; Sepúlveda et al., 2019) show that the tsunami hazard in the next 500 years for cities along the eastern coast of Hainan Island is negligible (wave height < 1 m). The only observed tsunami to have affected Hainan Island was generated by an offshore earthquake (Mw = 3.7) on 4 January 1992 and the struck south of the island, but the maximum tsunami wave, recorded in Yulin Bay, was only 0.78 m high (Ye et al., 1994). With few tsunami events and the widespread coastal lagoons and salt ponds (Song, 1984), Hainan Island is an ideal location for the creation and preservation of valuable storm archives of long-term scale.

Previous coring and geophysical studies indicate that lagoon deposits have considerable potential to provide meaningful information on past storm activity (Zhou et al., 2017). Here, we use sedimentary records from Xincun Lagoon, Hainan Island, China, to reconstruct the typhoon activity in the SCS during the mid–late Holocene, and to answer three main questions. (1) how has typhoon activity around the SCS changed over the mid–late Holocene? (2) is there a statistically significant relationship between ENSO and typhoon frequency in the SCS over centennial to millennial timescales? (3) what are the effects of different climatic regimes (e.g. ENSO and WPWP) on the SCS and even WNP typhoon activity?

2. Study areas and sites

Hainan Island is located in the northern SCS, to the west of the WNP. The oceanographic conditions around the island are characterized by a microtidal regime that is irregularly diurnal (Wang et al., 2001). A tropical monsoon climate prevails, with hot and rainy summers that contrast with mild and dry winters. When cyclones hit Hainan Island, they typically either head towards the east coast of the island or pass to the south and head towards Vietnam (Wang et al., 2001; Fig. 1a). This island lies further away from plate boundary and southern side of this island has been stable tectonically (Chen et al., 2015). Over the past 7000 yr in the northern SCS, sea level has been relatively stable (< 2 m; Baker et al., 2003; Zong, 2004; Shi et al., 2007; Yu et al., 2009b; Yao et al., 2013; Xiong et al., 2018).

Xincun Lagoon is one of the largest coastal lagoons on the southeastern coast of Hainan Island (Fig. 1). The present study site is located along the southeastern-facing shoreline and is vulnerable to intense storms arriving from the SCS and WNP. The bay covers 22.6 km^2 with a width of around 4.5 km and is separated from the open sea by granite hills (Nanwan Monkey Hill and Liuliang Hill), and exchanges water with the SCS through one narrow entrance (ca. 2 km long) in the southwest of the lagoon. This lagoon is located on the more tectonically stable south side of Hainan Island, where there are few active faults and little evidence of historical tsunami events (Chen, 1995; Zhou et al., 2017; Jiang et al., 2018). Two small streams drain into the tidal basin at a rate of approximately 1 m^3/s (The Compile Committee of China Bay Records, 1999). The modern sediments accumulating at the bottom of the lagoon are dominated by clay and silt (Yang et al., 2017a). The strongest winds and waves are from the southeast and east. Mean significant wave height is < 1 m, although during large storm condition it can reach about 4 m (Gong et al., 2008). Tidal variability is modest (mean range of 0.56 m), which minimizes the influence of dynamic tidal currents (Gong et al., 2008; Zhou et al., 2017).

3. Materials and methods

To reconstruct the depositional history of the lagoonal sediments in Xincun Bay, we acquired high-resolution seismic profiles, sediment cores, and geochronologies from the lagoon. The late Quaternary stratigraphy was mapped in October 2013 using a 3.5 kHz Geo-Pulse subbottom profiler (Geo-Acoustics, UK) coupled with a high-accuracy GPS (Trimble GPS SPS351). The penetration velocity of the transmitted signal was taken as 1600 m s^{-1}. The upper-most sedimentary unit (Unit 1) is approximately 5–10 m in thickness and seismic observations show no channel near the core sites of the lagoon within Unit 1 (Fig. 1c). The parallel and undisturbed stratigraphy of Unit 1 indicates a continuous sedimentary sequence within this upper unit (Fig. 1c).

A sediment core 5.8 m long (XCL-02, Fig. 2) was collected on January 20, 2016 using a drilling system equipped with a hydraulic piston

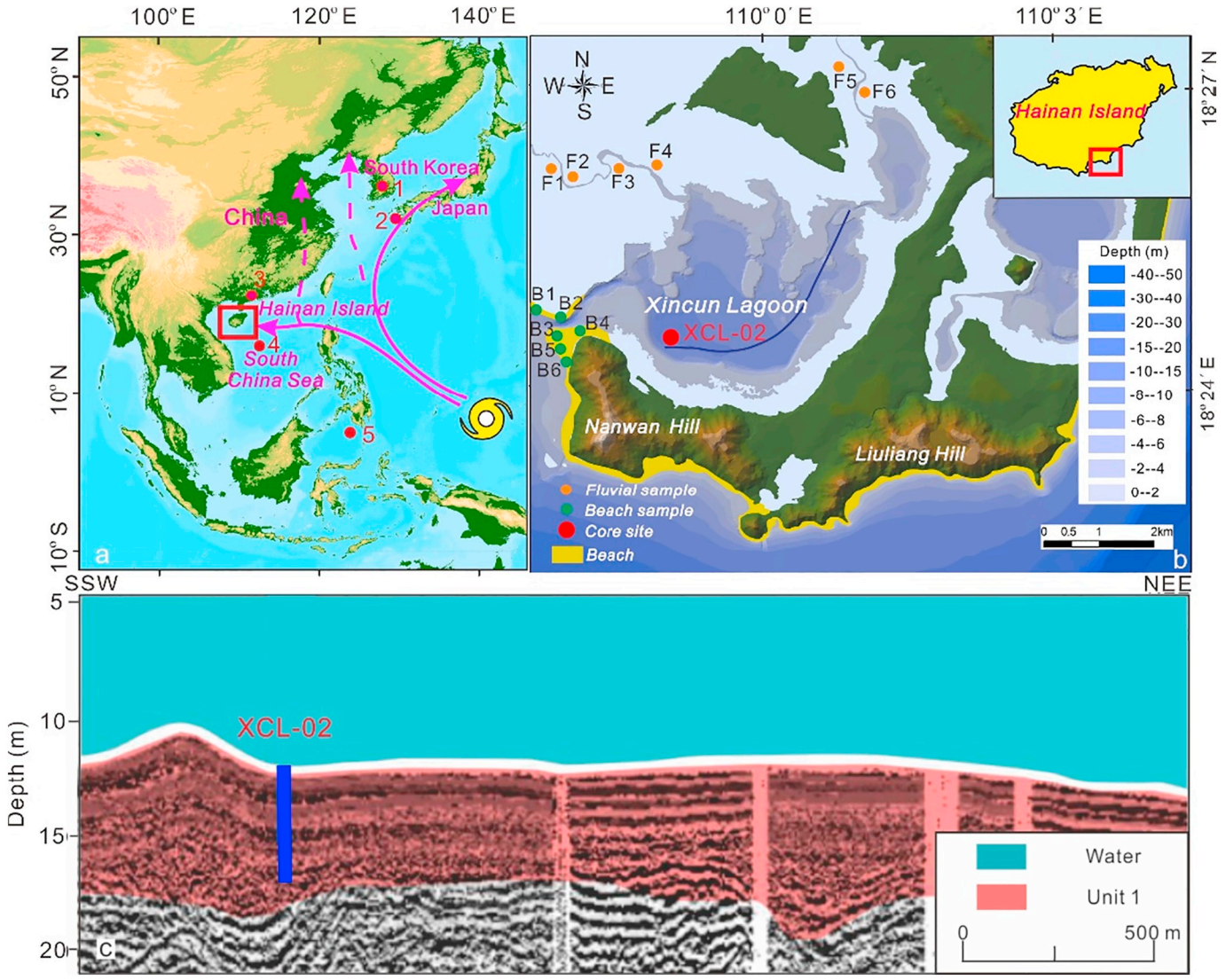

Fig. 1. (a) Map of the western North Pacific showing the study area (red square) in relation to the generalized tracks of TCs over the WNP over the past 50 years (modified from Chen et al., 2013). The locations of Korea (Yoo et al., 2015), Kamikoshiki Island, Japan (Woodruff et al., 2009), Guangdong Province (Liu et al., 2001), the Xisha Islands of SCS (Yue et al., 2019), and core MD98–2181 core (Stott et al., 2004) mentioned in text are identified by numbers1–5, respectively. (b) Maps showing the location of Xincun Lagoon on the southeast of Hainan Island (blue line) with bathymetry from chirp seismic survey lines, and location of core XCL-02 (red circle). (c) Seismic profile across the coring site. Blue dashed line indicates the location of core XCL-02. (For interpretation of the references to color in this figure legend, the reader is referred to the web version of this article.)

on a floating platform. Core XCL-02 (109°58′56.59″ E, 18°24′30.17″N) was collected at about 11 m lagoon water level (Fig. 1b). The core site was located > 2000 m from the entrance, and > 4500 m from the nearest tributary mouth (Fig. 1b). Surficial sediments were also sampled from the watershed of the Xincun lagoon and from the beach (12 samples in total; Fig. 1b), to identify the source of the coarse grained materials deposited in the tidal basin of Xincun Lagoon. The sediment cores were transported to the State Key Laboratory of Marine Environmental Science (Xiamen University) where they were refrigerated at 4 °C prior to being split, described, and photographed. Core XCL-02 was covered with a 4-μm-thick Ultralene film to avoid contamination of the Avaatech X-ray fluorescence core scanner (XRF) measurement unit and desiccation of the sediment (Richter et al., 2006). A halved core was run through a non-destructive, XRF to obtain a high-resolution down-core profile (at an interval of 2–5 mm) of the sediment's elemental composition (Hennekam and de Lange, 2012) and under two different tube voltage (for light elements: 0.1 mA, 10s count time, and 10 kV; for heavier ones: 0.75 mA, 45 s count time, and 30 kV). Only significant element contents (> 1000 cnts/s) are used. Reliable data were obtained for Al, Si, S, Na, K, Mg, Ca, Ti, Mn, Fe, Cu, Zn, Br, Sr, Rb, Zr, and Pb. Four powdered standards were analyzed every day before and after the analysis of the sediment cores to monitor signal drift, which showed that the signal remained stable during the analytical runs. In addition, the surficial sediments were subjected to geochemical analysis using a Panalytical PW230 X-ray fluorescence spectrometer (Zhang et al., 2015).

Grain size analysis of 1-cm sub-samples was conducted using a Mastersizer-2000 laser particle analyzer, which has a relative error of < 1% for replicate measurements (Jia et al., 2018). Each sample was measured three times and the repeatability of measurement was verified according to the statistics of the international standard ISO 13320-1. The GRADISTAT program version 4.0 (Blott, 2000) was used to calculate the sample statistics of the grain size distribution; i.e., mean grain size (*Mz*), sorting (*S*), standard deviation (σ), Skewness (*Sk*), and Kurtosis (*K*).

Dating of the sedimentary layers for the depth of (0–115 cm) was carried out using the ^{210}Pb and ^{137}Cs methods on a centennial timescale. Samples were dried at 60 °C for three days, and then sediment

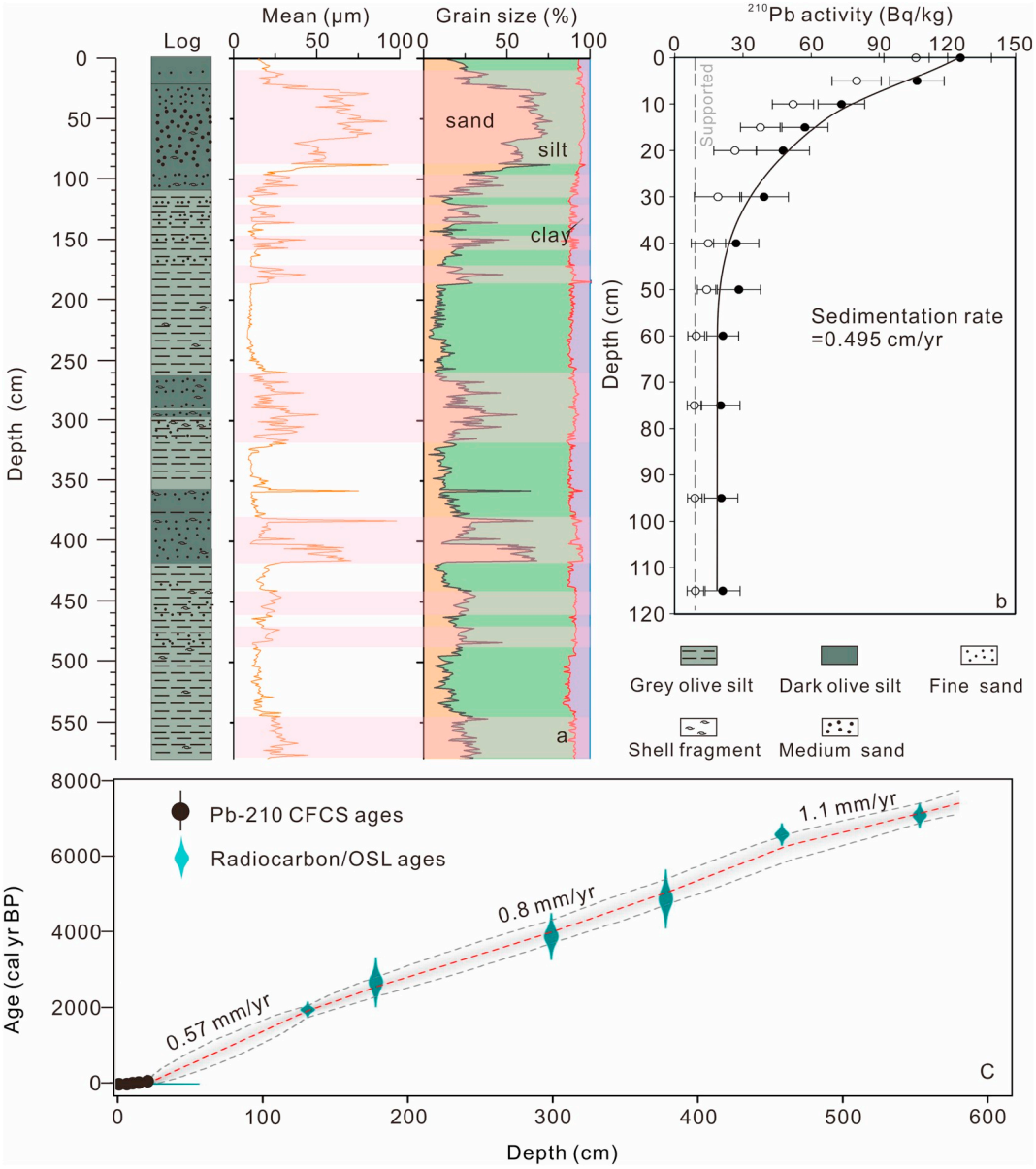

Fig. 2. (a) Lithology, mean grain size, sediment composition of sediment core XCL-02. The pink bars represent the 12 sand beds. (b) ^{210}Pb chronology for XCL-02 (the top part shows a ^{210}Pb profile for the upper 115 cm of XCL-02, circles and error bars show the measured ^{210}Pb activity and 2 sigma error range, and grey dashed line indicates level of supported ^{210}Pb in the sediment). (c) Age–depth profile of sediment core XCL-02 with age data and estimated sedimentation rates. The thick red line indicates single best model based on the weighted mean age for each depth. (For interpretation of the references to color in this figure legend, the reader is referred to the web version of this article.)

Table 1
Radiocarbon dates and OSL dates for Core XCL-02.

Sub-samples	Depth (cm)	^{14}C/OSL age (yr BP[a])	Cal yr BP (2σ) (yr BP[a])	Material	Method
XC-beta-01	131	2000 ± 30	1995–1875	Woody debris	AMS
XCOSL-01	175–180	2660 ± 185	2475–2845	Quartz	OSL-SAR
XCOSL-02	296–302	3870 ± 175	3595–4145	Quartz	OSL-SAR
XCOSL-03	375–380	4860 ± 440	4420–5300	Quartz	OSL-SAR
XC-beta-03	458	5810 ± 30	6650–6485	Charcoal	AMS
XC-beta-04	553	6240 ± 30	7165–6975	Charcoal	AMS

[a] "Present" is defined as 1950 CE by convention.

bulk dry density was calculated from the percent water content (Jia et al., 2012). After drying, sediment samples were filtered with an aperture of 63 μm to obtain fine sediments and sealed in a plastic box (70 × 70 mm) for three weeks. The ^{137}Cs and ^{210}Pb activities analyses by an HPGe γ-ray detector (Canberra Be3830). The activities of ^{210}Pb and ^{137}Cs were determined from the γ-ray peaks at 46.5 and 661.6 keV, respectively (Wang et al., 2016, 2017). The ^{210}Pbex activities were calculated by the subtraction of the activity of total ^{210}Pb and the activity of ^{226}Ra, determined using the γ lines at 351.9 keV for ^{214}Pb and $^{609.3}$ keV for 214Bi. The ^{210}Pb chronology was determined using the constant flux constant sedimentation (CFCS) model (Krishnaswamy et al., 1971).

The centennial- to millennial-scale chronologies were constrained using the accelerator mass spectrometry (AMS) ^{14}C and optically stimulated luminescence (OSL) dating methods. Three samples of plant material were sent to Beta Analytic for AMS radiocarbon dating (Table 1) and the calibrated age ranges were determined using the IntCal13 dataset (Reimer et al., 2013), where "Present" is defined as 1950 CE by convention. To complement the radiocarbon dating results,

three OSL ages were obtained from quartz grains of the 40–63 μm fraction using the single-aliquot regenerative (SAR) -dose protocol (Murray and Wintle, 2000). The OSL sampling was undertaken in the TL/OSL dating laboratory of Shaanxi Normal University, China under subdued red-orange light. Luminescence measurements for OSL samples were conducted on a Risø-TL/20 reader equipped with a $^{90}Sr/^{90}Y$ beta source. For each of the OSL samples, 20 aliquots were measured. The contents of U, Th, and K in the samples was measured by neutron activation analysis at the China Institute of Atomic Energy in Beijing, China. The OSL ages were determined using the program Age.exe (Grün, 2003). The equivalent doses (*De*) for all OSL samples showed an asymmetric distribution (Fig. S1), which based on the age and depositional environment, was most probably caused by partial bleaching. To avoid overestimation of the OSL ages due to this partial bleaching, the OSL ages were interpreted using a Minimum Age Model (MAM), adapted from Olley et al. (1998), and were calibrated to ages before 1950 CE (Table 1), as reported previously by Zhou et al. (2016). Finally, the chronology of the core XCL-02 was produced using the Bayesian model Bacon program (Blaauw and Christen, 2011).

4. Results

4.1. Stratigraphy and chronology

The uppermost 10 m of the sediments deposited within Xincun Lagoon are characterized by laminated, parallel to subparallel seismic reflectors (Fig. 1c). Core XCL-02 was primarily composed of a grey mud that contained intercalations of coarser grained (sandy) deposits. Based on lithology, grain size, and chronostratigraphy, we divided core XCL-02 into three units in ascending order as follows.

4.1.1. Lower unit (580–110 cm)

This unit comprises greenish-grey silt interbedded with layers of coarser grained deposits or mixed coarse sand and shell fragments (Figs. 2, 3). Silt (27.66% to 86.13%) is dominant, followed by sand (2.92% to 68.09%) and clay (4.17% to 14.79%). The mean grain size is between 8.05 and 75.12 μm (overall average 15.90 μm). The coarser grained layers generally consist of rounded sand-sized siliciclastic grains interspersed with calcium carbonate shells and shell fragments (Figs. 2, 3). Most of these coarser layers have a low proportion of organic material and grade from olive grey to grey or black in colour, with some showing fine-scale laminations (1–2 mm) and lenticular bodies (Figs. 2, 3). Several sand beds occur within the non-laminated coarser grained units (Figs. 2, 3), which may suggest deposition by multiple events. The fine grained mud with homogeneous sediment structure (Fig. 3) indicated that the core areas were experiencing weak resuspension in the tidal basin during this stage. Lenticular bedding, wavy bedding, parallel lamination (Fig. 3) are common in some coarse grain layers.

The basal mud at 5.53 m in core XCL-02 was dated to ca. 7000 cal yr BP, which supports the interpretation that the 5.8 m sediment sequence accumulated during the mid-to-late Holocene. An age of 6568 ± 83 cal yr BP at 458 cm depth was obtained from AMS ^{14}C dating of charcoal. A charcoal sample from a depth of 131 cm was dated to 1935 ± 60 cal yr BP. Therefore, the sedimentation rate between 131 and 458 cm in the middle unit of the core was calculated to be approximately 0.8 mm/yr (Fig. 2c). Ages of 2660 ± 185 cal yr BP at 175–180 cm, 3870 ± 175 cal yr BP at 296–312 cm, and 4860 ± 440 cal yr BP at 375–380 cm depth obtained using OSL dating also support our calculated sedimentation rate. These two ^{14}C and three OSL ages indicate that this unit was deposited mainly between 7000 and 2000 cal yr BP.

4.1.2. Middle unit (110–20 cm)

This unit consists mainly of a grey to light grey sandy mud (Figs. 2, 3). The sand content is between 15.72% and 77.14%, silt between 20.04% and 72.37%, and clay between 2.83% and 11.92%. The mean grain size is 11.99–93.14 μm (overall average 52.02 μm). This sandy mud, together with the presence of rip-up clasts (Fig. 3b), reflects a high-energy depositional environment with significant resuspension (Chen et al., 2000; Wang et al., 2010, 2012).

4.1.3. Upper unit (20–0 cm)

This unit is characterized by yellowish-grey silt interbedded with laminated thin sand layers. The silt content is 56.75% to 78.81%, and the clay and sand contents are 4.49% to 7.82% and 14.46% to 38.77%, respectively. The sand layers are generally thin (1–2 mm) in the *upper unit*. The mean grain size (20.52 μm) is finer than in the underlying

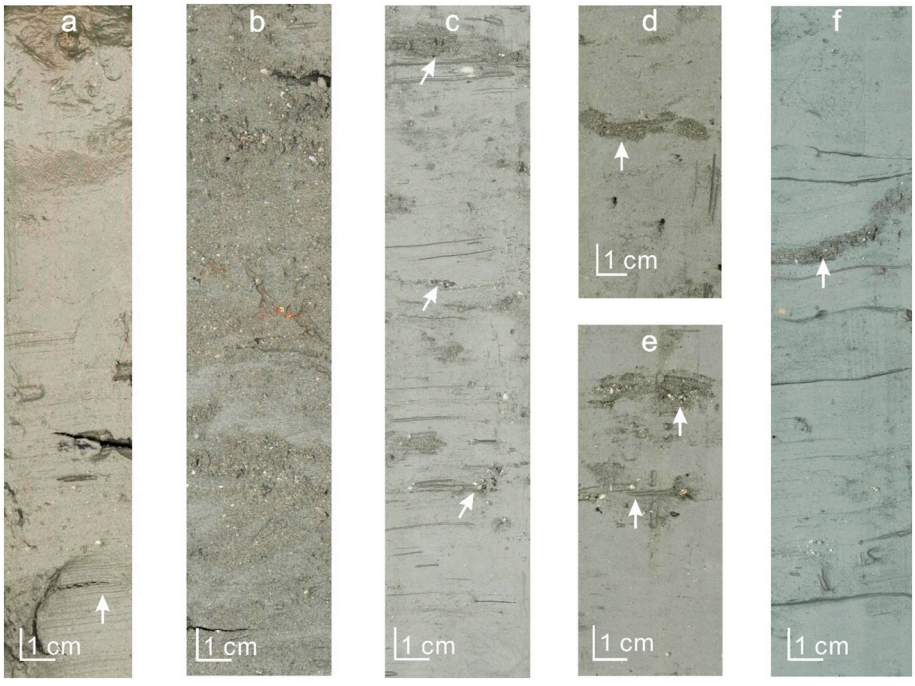

Fig. 3. Core photographs of typical sedimentary facies in core XCL-02; (a) 0–20 cm: fining-upward mud underlain by finely laminated coarse silt layers. (b) 40–60 cm: structureless sandy-mud mixed with abundant shell fragments and mud rip-up clasts. (c-f) examples of sandy facies interbedded with homogeneous mud-dominated deposits: (c) thick and thin sand layers (450–470 cm), (d) lenticular body (350–360 cm), (e) laminated sand layer (170–180 cm), and (f) wavy (270–290 cm) sand layers.

Table 2
Lead-210 data used to determine the relation between sediment age and depth.

Depth (cm)	^{210}Pb activity (dpm/g)		Mass depth (kg/m^2)	Calibrated age (cal yr BP)
	Total	Unsupported		
0–1	2.1 ± 0.2	1.8 ± 0.2	1.1	−63 ± 1
4–5	1.8 ± 0.2	1.3 ± 0.2	5.7	−55 ± 1
9–10	1.2 ± 0.2	0.9 ± 0.2	11.5	−45 ± 2
14–15	1.0 ± 0.2	0.6 ± 0.1	17.4	−35 ± 3
19–20	0.8 ± 0.2	0.44 ± 0.2	23.3	−25 ± 4
29–30	0.7 ± 0.2	0.32 ± 0.2	36.6	
39–40	0.4 ± 0.2	0.25 ± 0.1	50.2	
49–50	0.5 ± 0.2	0.23 ± 0.1	63.7	
59–60	0.4 ± 0.1	0.16 ± 0.1	78.2	
74–75	0.3 ± 0.1	0.1 ± 0.1	99.8	
94–95	0.3 ± 0.1	0.1 ± 0.1	130.6	
114–115	0.4 ± 0.1	0.2 ± 0.1	158.2	

middle unit (Fig. 2). This fining-upwards trend may reflect a decrease in the energy of the depositional environment and hence resuspension during this period. We suggest that this was caused mainly by increases in aquaculture and coastal construction in recent decades (Zhou et al., 2017), which have led to a reduction in the tidal prism and lower flow velocities (Yang et al., 2017a).

Because the ^{137}Cs activity in majority samples was below the detection limit (0.5 Bq/kg), we were unable to obtain a reasonable ^{137}Cs profile. The excess ^{210}Pb profile shows an exponential decay with depth (Fig. 2b). Below 20 cm depth where the sharp changes in the value of excess ^{210}Pb occurred, the ^{210}Pb activity remained largely steady (Table 2), representing the background value. The ^{210}Pb ages indicate that *the upper unit* of the core was deposited between about −25 cal yr BP and the present (Fig. 2, Table 2).

4.2. Grain size

The grain size analysis (Table 3; Fig. 4a) of beach samples B1-B6 show unimodal distributions with mean grain size of 280.85–324.08 μm, indicating well sorted fine to medium sand sediments (Folk and Ward, 1957). The fluvial samples (F1–F6) came from the two small streams. It is assigned as the fluvial source. Fig. 4a shows that the fluvial sediments have unimodal to multimodal distributions with a mean grain size in the range of 17.04–76.99 μm. These deposits are a poorly sorted fine silt to very fine sand sediments, which reflects the relatively short distance of transportation along the two short streams. These fluvial surface sediment samples show a generally decrease in the grain size from upstream to downstream through the river watershed (Table 3; Fig. 4a).

As the dominant sediments in this core are silts, and the mean percentage of the > 63 μm fraction of this core is 24.08 ± 0.7%, we interpreted subsamples with > 24 ± 0.7% sand (> 63 μm) as

Table 3
Grain-size distributions of the surface samples from the fluvial (F1-F6) and beach (B1-B5) sediments of Xincun Lagoon.

Sample name	Mean (μm)	Md (μm)	Sorting	Skewness	Kurtosis
F1	62.88	66.12	1.72	−0.12	1.23
F2	44.12	61.78	3.55	−0.44	1.13
F3	75.28	69.52	2.14	0.20	1.31
F4	17.04	17.89	3.62	−0.11	0.97
F5	76.99	71.32	2.12	0.19	1.34
F6	35.49	43.67	3.38	−0.27	1.02
B1	290.28	285.10	1.43	0.10	1.01
B2	297.22	285.13	1.58	0.22	1.18
B3	280.85	267.20	1.56	0.20	1.06
B4	281.35	275.34	1.41	0.13	1.06
B5	324.08	299.55	1.62	0.27	1.01

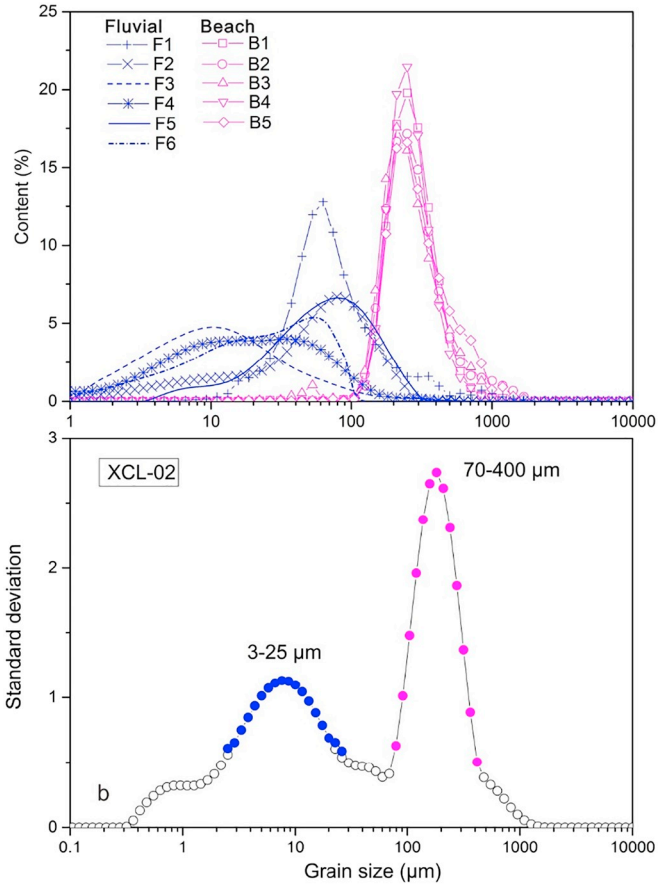

Fig. 4. (a) Grain-size distributions of representative samples of river (F1-F6) and beach (B1-B6) sediments from Xincun Lagoon. (b) Standard deviation vs grain size diagram for XCL-02 with blue and pink dots representing the part of the grain size distribution with the highest variability between 3 and 25 μm, and between 70 and 400 μm, respectively. (For interpretation of the references to color in this figure legend, the reader is referred to the web version of this article.)

indicating high-energy depositional events (Fig. 2a). Nine prominent shifts in grain size are apparent in the core (Fig. 2a). Throughout the *lower unit* (110–580 cm), eight sand peaks are evident, and the average percentage of sand is 27.81% (24.1% to 38.2%). In the *middle* (20–110 cm) and *upper units* (0–20 cm), two sand peaks are evident, and the average percentage of sand are 30.87% and 55.91%, respectively (Fig. 2a).

The "grain size versus standard deviation" method, based on calculating the standard deviation for each grain size class of the grain size distribution, was used to identify the grain size intervals with the highest variability (Fig. 4b; Boulay et al., 2003). The standard deviation quantifies the variability around the mean. Using this method, it is possible to determine the grain size classes that were most sensitive to changes in the sedimentary environment through time (Sun et al., 2003; Sabatier et al., 2008; Degeai et al., 2015). The standard deviation versus grain size classes for core XCL-02 are displayed in Fig. 4b. The two main grain size populations that show the highest variability (standard deviation ≥0.6) are 3–25 μm (clay to medium silt) and 70–400 μm (fine sand to medium sand). This means that the percentage of > 63 μm fraction can be used as a proxy to detect inputs of the coarser deposits into the lagoon (e.g. Switzer et al., 2005).

The fine grained sediment sequence is interbedded with 10 coarser beds (Fig. 2a, pink and red bands in Fig. 5). The main peaks in grain size (i.e. > 63 μm fraction) in the core occur at depths of 545–580, 470–485, 440–460, 380–410, 260–315, 170–185, 145–155, 120–135, 95–115, and 10–85 cm. These average peak values of the > 63 μm

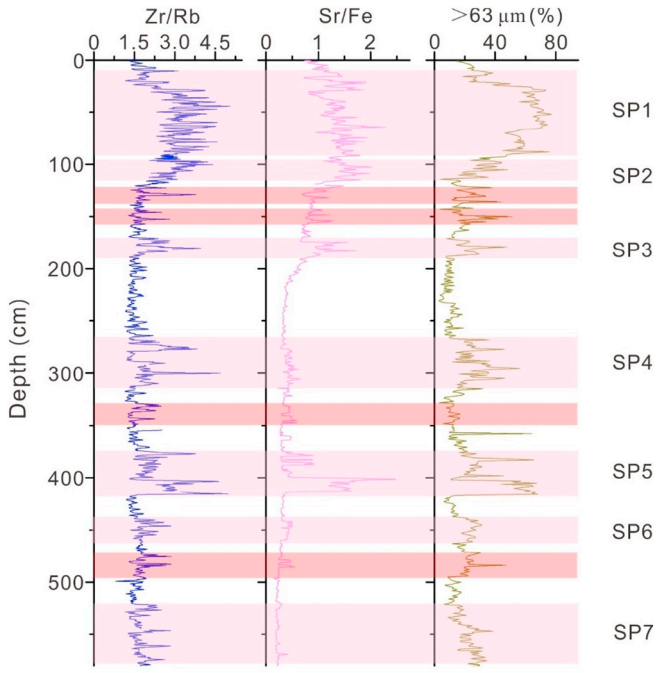

Fig. 5. Identification of paleostorm events based on grain size and geochemical inter-element ratios. The identified events show a dominated by the > 63 μm sand fraction, and peaks in Zr/Rb and Sr/Fe ratios. The red horizontal bars representing these peaks cannot associated with storm deposits. The pink horizontal bars represent the seven storm periods (SP1–SP7) identified from the XCL-02 sequence since 7500 cal yr BP. (For interpretation of the references to color in this figure legend, the reader is referred to the web version of this article.)

fraction range from 25.13% to 55.91% and the maximum value (77.14%) was found around 52 cm depth.

4.3. Geochemistry

Twelve geochemical data sets of surficial samples (Ti, Fe, Sr, Ca, Cu, Zn, Zr, Mn, Co, As, Rb, and Pb) were obtained using an X-ray fluorescence spectrometer. Variations in the concentrations of the most important elements shows that the elemental composition of the beach sediments is enriched in Sr, Zr, and CaO, depleted in Fe_2O_3, TiO_2, MnO and Rb (Fig. 6). On the contrary, fluvial sediments is enriched in Fe_2O_3, TiO_2, MnO, Al_2O_3, and Rb. Similarly, Pe-Piper et al. (2016) reported that river sediments from eastern Hainan Island characterized by K_2O (2.51% to 3.08%), TiO_2 (0.29% to 2.89%), Fe_2O_3 (0.85% to 4.73%) and Rb (77–96 ppm), whereas the sandy beach deposits are characterized by Zr (286–15,400 ppm), CaO (0.19% to 19.51%), and Sr (36–1509 ppm). Although our results were based on a limited number of samples and detected elements, they are in agreement with previous studies in the area (Zhu et al., 2004; Wang et al., 2017b).

Down-core profiles of Sr, Zr, Ca, Al, Fe, Rb, Ti, and Mn can also be used to identify or delineate the different sedimentological units (Fig. 7). As with the geochemical results for the surficial sediments, we were able to identify two element groups in core XCL-02. The first group comprises Al, Fe, Rb, Ti, and Mn, which exhibit similar variations. The contents of this first group of elements are higher in the finer grained intervals than in the coarser layers. This group shows relatively high base levels in the *lower* (below 110 cm) and *upper* (above 20 cm) *units,* and lower base levels in the *middle unit* (Fig. 7). The contents of Al, Fe, Rb, Ti, and Mn vary within the ranges 288–16,347, 20,076–140,453, 2298–14,035, 1663–19,992, and 256–2765 cnts, respectively, and have average values of 10,262, 98,842, 9759, 13,273, and 1140 cnts, respectively. The second group comprises Sr, Zr, and Ca, and displays a different behavior to the first group (Fig. 7). These three elements are relatively enriched in the coarser grained intervals; i.e., the *middle unit* (20–110 cm). The contents of Zr, Sr, and Ca are within the ranges 4173–60,188, 12,185–108,254, and 4885–321,182 cnts, respectively, with averages of 18,785, 42,529, and 103,070 cnts, respectively.

Inter-element ratios can be used to trace storm deposits geochemically (Dezileau et al., 2011, 2016; Sabatier et al., 2012; Raji et al., 2015). In this study, only interelement ratios which present the most important variations through depth were selected. And we chose the ratio Zr/Rb and Sr/Fe, which also have been widely used to distinguish the marine and fluvial source (e.g. May et al., 2012; Degeai et al., 2015; Raji et al., 2015). As shown in Fig. 5, we can find relatively stable base values of Zr/Rb and Sr/Fe ratios vary from 1.0 to 1.6 and 0.5–1.0, respectively, in the *lower unit* (below 110 cm). Between 20 cm and 110 cm depth, the Zr/Rb and Sr/Fe ratios base values increase to 2–3 and 1.5–2, respectively. Above the 20 cm, the Zr/Rb and Sr/Fe ratios base value around 1.5 and 1.0 respectively.

As the mean values of the Zr/Rb and Sr/Fe ratios were 1.97 ± 0.4 and 0.71 ± 0.1, respectively, we interpreted the positive anomalies in the Zr/Rb and Sr/Fe ratios (i.e. > 1.97 ± 0.4 and 0.71 ± 0.1, respectively; Fig. 5) as indicating "high-energy" events. The Zr/Rb and Sr/Fe ratios are high mainly in the nine coarse grained intervals along the XCL-02 sequence (Fig. 5). These high values of Zr/Rb and Sr/Fe ratios vary from 1.94 to 5.28 and 0.74 to 2.48. The maximum value is found around 46 cm (Zr/Rb) and 405 cm (Sr/Fe), respectively. Throughout the *lower unit* (110–580 cm), six Zr/Rb peaks and four Sr/Fe peaks are evident and the average values of the Zr/Rb and Sr/Fe ratios are within the ranges 1.94–2.42, and 0.87–1.14, respectively. In the *middle* (20–110 cm) and *upper units* (0–20 cm), two Zr/Rb peaks and Sr/Fe peaks are both evident, and the average values are increase to 2.79–3.32 (Zr/Rb) and 1.33–1.56 (Sr/Fe), respectively. The main peaks of Zr/Rb and Sr/Fe ratios in the core occur at depths of 547–580, 440–460, 380–415, 340–350, 260–315, 170–185, 95–115, 10–85 cm, and 380–415, 170–185, 140–155, 120–135, 95–115, 10–85 cm, respectively (Fig. 5).

5. Discussion

5.1. Age–depth model for core XCL-02

The chronology of the core XCL-02 was established by combining the ^{210}Pb ages, OSL dating results and the calibrated AMS ^{14}C ages (Fig. 2; Tables 1, 2).

The silty mud that dominates in the upper 20 cm of this unit indicates that the sedimentary environment for this unit was characterized by a relatively constant accumulation rate. Below the top 20 cm, the excess activity (< 0.4 dpm/g) was too low to determine a sedimentation rate (Table 2), and this suggest that the sedimentation rate had decreased significantly. This is supported by the changed in lithostratigraphy (Figs. 2a, 3) and sedimentation rate (Figs. 2b, c) in the *middle unit*. The structureless fine–medium sand dominates there, mixed with abundant shell fragments and mud rip-up clasts, reflecting a high-energy, dynamic depositional environment. In this context, we suggest that during this higher energy phase some of deposits may have been eroded and hence leading to a decreased sediment accumulation rate in the depositional sequence. Therefore, the ^{210}Pb chronology of the top 20 cm of the core was determined using the CFCS model, which have been widely used in this type of environment (Sabatier et al., 2008; Zonta et al., 2018). ^{210}Pb chronologies calculated for XCL-02 using the CFCS model are illustrated in Fig. 2b, c and Table 2.

Below 20 cm, the chronology of the core XCL-02 were constructed with the Bayesian model Bacon program (Blaauw and Christen, 2011), using the calibrated AMS ^{14}C ages and OSL dating results and ^{210}Pb-derived sedimentation age at 20 cm depth (Fig. 2; Table 2). A Bacon prior value of accumulation rate of 10 yr/cm was chosen based on the

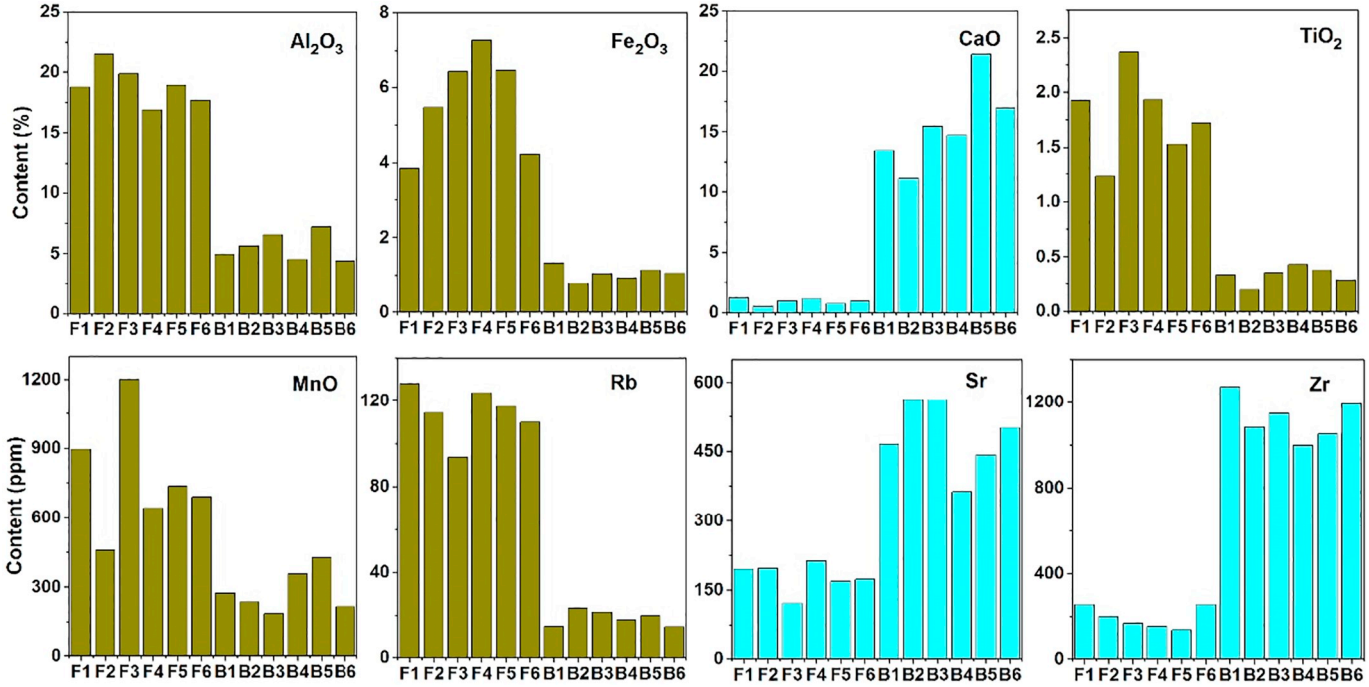

Fig. 6. Element contents in the fluvial (F) and beach (B) sediments. The fluvial sediments (F1-F6) are characterized by higher content of Al_2O_3, Fe_2O3, TiO_2, MnO and Rb, while the beach sediments (B1-B6) are enriched in CaO, Sr and Zr.

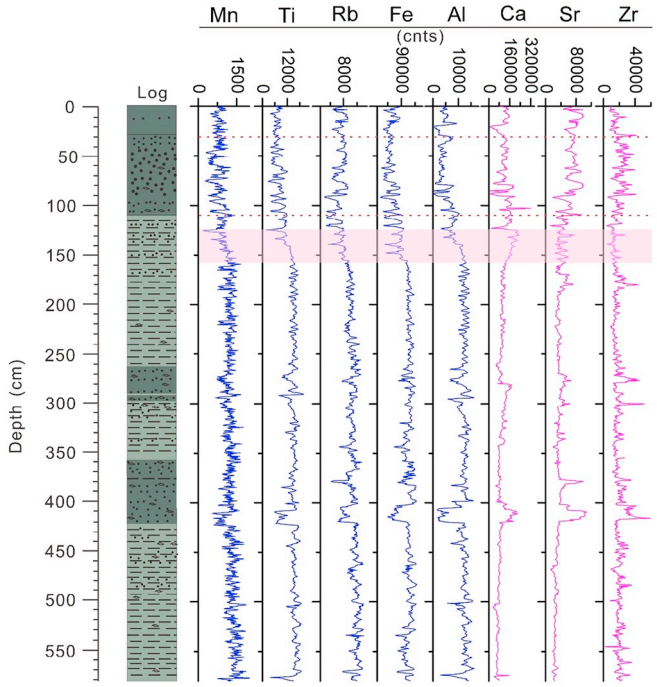

Fig. 7. Records of eight geochemical elements versus depth in core XCL-02. The pink horizontal bars represents an interval of Ca and Sr peaks associated with low Zr values, possibly originating from lagoonal biogenic productivity. (For interpretation of the references to color in this figure legend, the reader is referred to the web version of this article.)

average growth rate of about 1 mm/yr for below 20 cm of XCL-02 (Fig. 2c). The posterior of the accumulation rate is in good agreement with their prior (Fig. 2c), suggesting that our choice for the prior value is reasonable. The posterior age model produced using Bacon provides an age near the base of the core of between 7106 and 7724 cal yr BP and has a maximum uncertainty of 381 years (95% confidence interval) and an average uncertainty of 308 years (95% confidence interval) (Fig. 2c). The timing of the sediment core XCL-02 lithological changes are consistent with abrupt changes in average sedimentation rate (Figs. 2, 3). We can see that the first major slope change occurs between approximately 6200 cal yr BP and 7400 cal yr BP (Fig. 2c), and a high accumulation rate (~1.1 mm/yr) could be seen in the profile. This rate is the highest recorded in core XCL-02 and might be related to a significant increase in sediment input caused by sea level rise (Zong, 2004; Shi et al., 2007). The second synchronous slope change at about 1850 cal yr BP in XCL-02 can be attributed to enhanced hydrodynamic condition, resulted in some erosion of the deposits and low sediment accumulation rate.

We thus used the ^{210}Pb CRS ages, OSL ages and the calibrated AMS ^{14}C ages to develop an age-depth model by Bacon age model (Fig. 2c). Ages of −25, 1540, and 7393 cal yr BP were then obtained by the model for core depth 20 cm, 110 cm, 580 cm where sedimentary facies changed (Fig. 2b, c).

5.2. Site sensitivity through time and storm deposit signature

5.2.1. Site sensitivity through time

Sea-level rise, as well as changes to barrier morphology, sediment supply, and storm activity, can all potentially influence the sensitivity to record storms in backbarrier settings (Scileppi and Donnelly, 2007; Sabatier et al., 2012; Woodruff et al., 2013).

Sea-level rise (fall) can affect the sensitivity of coastal lagoon to record storms by moving the shoreline farther inland (seaward) and narrowing (widening) the barrier beach through time. In this context, an increase or decrease in sand layer through time can be caused solely by a sea-level change. However, since 7500 yr BP in the northern SCS, sea level fluctuations have been relatively small (< 2 m; Baker et al., 2003; Zong, 2004; Shi et al., 2007; Yu et al., 2009b; Xiong et al., 2018). Although Yao et al. (2009) and Zhang et al. (2008) reported evidence of higher sea levels and argued that the whole of the tectonic uplift of Hainan Island might have occurred since the late Pleistocene to middle Holocene, Jiang et al., 2018 showed that the higher sea levels in the eastern Hainan Island could have been the result of TC activity in the

area. Moreover, the Xincun lagoon is almost blocked by Nanwan Hill (Fig. 1b), and the barriers fronting our study site have remained largely stable since the middle Holocene (The Compiling Committee of China Bay Records, 1999; Zhao et al., 1999). Thus, the abrupt increase in coarse-grained deposition after ca. 7000 yr BP cannot be explained by changes in relative sea levels.

The movement of the tidal inlet can also affect the sensitivity of a particular area to storm-induced deposition. Storm energy could have more easily penetrated into a particular area of the back-barrier environment if an inlet moved closer to the core site. Remote sensing and hydrodynamic survey data acquired since the 1980s clearly show that the tidal inlet is relatively stable (Gong et al., 2008), although the position of the main ebb tidal channel shows a cyclic shift. Furthermore, the direction of longshore drift near the inlet is from east to west (Gong et al., 2008), which suggest that the inlet should have moved gradually to the west, as indicated by Gao et al. (2004). However, the inlet position is now close to the eastern stable bedrock, suggesting the position of the inlet is relatively stable over the study period. This conclusion is supported by the previous geological and geomorphological surveys of late Quaternary in the Xincun Lagoon (Song, 1984; Zhao et al., 1999). In general, the site morphology and limited sea level rise over the past 7000 years indicate a relatively stable barrier system (Zong, 2004; Shi et al., 2007; Jiang et al., 2018).

A human-induced decrease in sediment supply to the coast was an additional cause of the degradation of barrier beaches at the study sites, which lead to the observed increase in storm-induced flooding. However, widespread deforestation in the region since the Ming-Qing dynasties (ca. 600–200 cal yr BP; Zhou et al., 2017) is thought to have increased, rather than decreased, sediment delivery to the coast (Jia et al., 2012; Zhou et al., 2017). It is possible that background increases in grain size at the present study site were caused by soil erosion associated with extreme rainfall events. However, our surface sediment analysis clearly shows that peaks in grain-size above this background rise were more likely to have been caused by coarser marine sediments derived from higher-energy coastal events, rather than increased inputs of fluvial deposits generated by land clearance (see Section 4.2). Thus, changes in sediment supply cannot explain the observed increase in storm deposition since 1700 cal yr BP (Fig. 9a). A recent reconstruction of storms that have struck the Xisha Islands in the SCS also provides clear evidence for an increase in regional storminess since 1800 cal yr BP (Yue et al., 2019; Fig. 9c), which might explain the increase in storm-induced coarse-grained deposits since 1700 cal yr BP.

The record of past storm activity can be complicated by various coastal dynamics. However, the organic-rich mud sediment types and uniform deposition rate that persisted the record show that these areas were experiencing quiescent sedimentation, at least over the period of 7000–2000 yr BP (Figs. 1c, 2), indicating that the sedimentary environment at the study site was relatively stable over that time. However, layers of sandy-mud are present throughout the record of the past ~2000 years, and this sedimentary record consistent with historically documented typhoons and storm reconstructions across the northern SCS (Figs. 8, 9) and indicate that the changes in the Xincun Lagoon proxies (i.e., grain size and Zr/Rb) in the XCL-02 record mainly the passage of intense storms passing by Hainan Island over the past 2000 years. In brief, the various lines of evidence presented in this study tend to indicate that the Xincun Lagoon site is relatively sensitive to record storm events passing by the Hainan Island.

5.2.2. Storm deposit signature

Grain size and geochemical results of the surficial sediments shows that the high percentage of coarse sediments are source from the sandy beach, whereas sediments from the river watershed have a finer grain size (Table 2, Figs. 4, 5). This could be explained by the fact that rivers provide the fine fraction of the lagoon sediments whereas the marine inputs are characterized by coarse sands (Yang et al., 2017a). Core XCL-02 is composed of clay and silt interbedded with dark grey, coarser

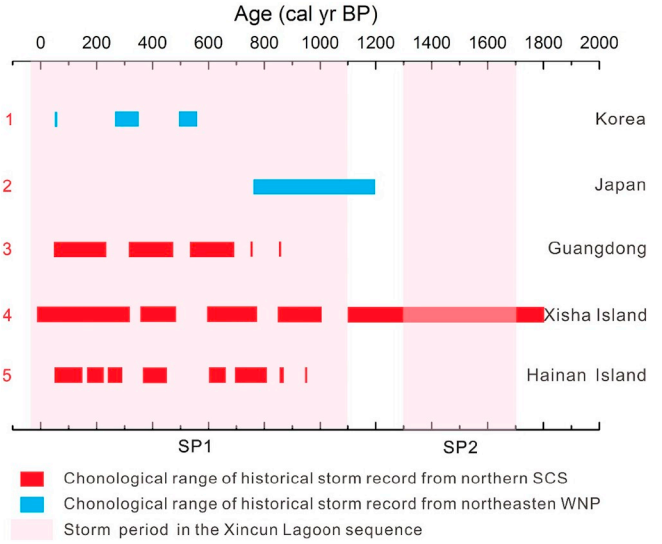

Fig. 8. Comparison of storm activity at Xincun lagoon with paleostorm records around the SCS for the past 2000 years. (1) Frequency of typhoon events in Korea derived from documentary records (Yoo et al., 2015). (2) Proxy records of storm-induced sedimentation from Kamikoshiki, Japan. (3) Historical storm records from written sources for Guangdong Province (Chen, 1995; Liu et al., 2001). (4) Proxy record of storm-induced deposition from the Xisha Islands in the SCS (Yue et al., 2019). (5) Historical storm records from written sources for Hainan Island.

grained layers of siliciclastic sand and shell fragments (Figs. 2, 3). The percentage of sand (> 63 μm fraction) was used as a proxy to detect the coarser detrital inputs to the lagoon. According to Fig. 2 and Fig. 5, the fine grained sediment sequence is interbedded with 8 coarser-beds (Figs. 2, 5). According to the obvious differences in the surficial sediments (Fig. 6), Zr/Rb and Sr/Fe ratios were further calculated for core sediments. The Zr/Rb and Sr/Fe ratios exhibit similar variations to the percentage of sand (> 63 μm), with the values being high mainly in the coarser intervals and low in the finer intervals (Fig. 5). The evolution with depth of the two ratios displays 9 main changes in the core XCL-02.

During weathering, zircon maintains its original morphology, as do other stable minerals such as quartz, and these minerals tend to be relatively concentrated in the coarser fraction of detrital deposits. Rb in all kinds of rocks is found dispersed mainly in minerals containing K, such as biotite, muscovite, feldspar, and illite, and tends to be concentrated in clay minerals. Thus, the Zr/Rb ratio reflects the content of coarse minerals relative to clay minerals, and is often used as a proxy for sedimentary environment in hydrological events research (Guilizzoni et al., 2006; Wang et al., 2011; Jones et al., 2012). The Zr/Rb ratios are high in the high percentage of sand (> 63 μm) intervals. This probably suggests that their highest values are related to storm coarse-grained sediment inputs into the lagoon. Additionally, the similar patterns seen in the downcore profiles of the Zr/Rb ratio and coarser sand layers (Fig. 5) indicate that the Zr/Rb ratio can also serve as a good proxy for paleostorm events recorded in a lagoonal sedimentary sequence.

In previous studies of paleostorms, high Sr concentrations have been associated with either carbonate shells from sand-barriers or a high proportion of shells within the lagoonal sediments related to the biogenic content (Sabatier et al., 2010; Degeai et al., 2015). It is important to distinguish between those shells derived from coastal and nearshore barriers, and those from intralagoonal biogenic productivity. To this end, a crossover study of the Sr content, Ca content, and Zr/Rb ratio of the sediments may provide additional information. Consequently, the shelly layers with high Sr/Fe and Ca peaks only (i.e., without Zr/Rb peaks) will probably be related to mollusc shells from a lagoonal fauna

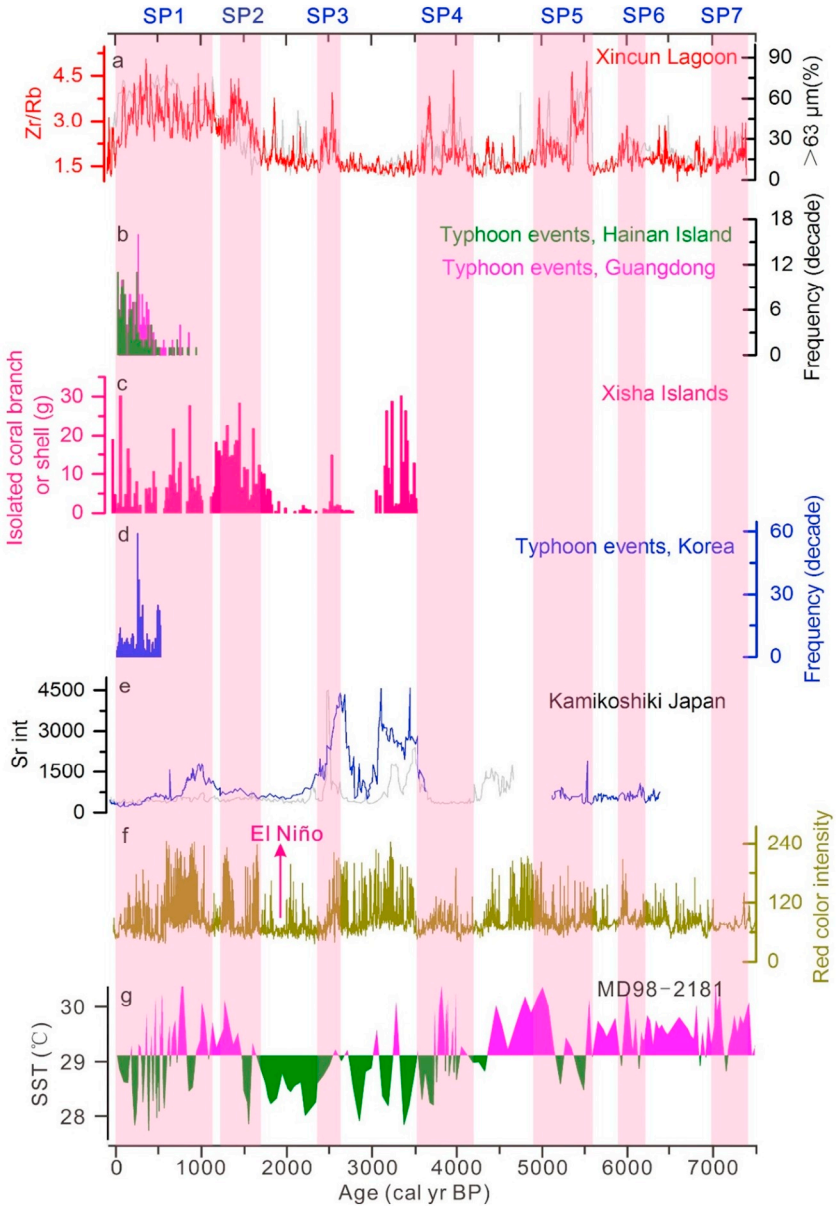

Fig. 9. Time series comparisons. (a) Zr/Rb ratio and coarse sediment content from core XCL-02. (b) Historical storm records from written sources for Hainan Island and Guangdong Province (Chen, 1995; Liu et al., 2001). (c) Sediment archive of storm-induced coarser grained materials from a coral reef lagoon in Xisha Islands, SCS (Yue et al., 2019). (d) Frequency of typhoon events in Korean derived from the documentary records (Yoo et al., 2015). (e) Sr time-series of storm-induced sedimentation for cores NKI5 (blue) and KI2 (grey) from Kamikoshiki, Japan (Woodruff et al., 2009). (f) Red colour intensity of sediment from the equatorial Pacific (Moy et al., 2002). (g) SST from core MD98–2181 (Stott et al., 2004). The pink bars indicate storm periods, as inferred in this study. (For interpretation of the references to color in this figure legend, the reader is referred to the web version of this article.)

developed in finer clayey deposits, as proposed by Sabatier et al. (2010).

Thus, we also present the Ca content, Sr/Fe and Zr/Rb ratios to detect the storm deposits.

Taking into account the geochemical signature of the sedimentary sources in the watershed and the coastal beaches around the Xincun Lagoon, the sedimentological signature of the storm events preserved within the XCL-02 sequence is characterized by a coarser particle size and high Zr/Rb and Sr/Fe ratio peaks. If proxies show peaks in grain size and Sr/Fe ratio (without Ca peak), this would indicate more coarse grained sediment mixed with shell or algal material from the beach and nearshore areas during storm events.

5.3. Reconstruction of paleostorm frequency in Xincun lagoon

5.3.1. Paleostorm frequency and duration of storm periods in Xincun Lagoon

Based on the characteristics of storm event deposits described above (Section 5.2), we use the Zr/Rb and Sr/Fe ratios, as well as the percentage of sand (> 63 μm) in the sediments, to identify the storm deposits (Figs. 5, 9). A total of seven storm deposit beds (SP1 to SP7) were identified (Figs. 5, 9). These storm deposit beds were systematically associated with a high Zr/Rb ratio and coarser grain size. However, the Sr/Fe peak at the depth of 120–135 cm and 145–155 cm did not correlated with the Zr/Rb ratio peak (red bar; Fig. 5). This Sr/Fe peak could have been caused by the stronger development of an in situ lagoonal micro-fauna, because increased amounts of Ca were also evident at the same depth (red bars in Figs. 5, 7). Thus, this abnormally Sr-rich coarse bed at the depth of 120–135 cm and 145–155 cm were not considered to be a storm deposit. In addition, the Zr/Rb peak at 340–350 cm depth coincides with a fine grain size level (Fig. 5). We might interpret this bed as reworked sediments from the intralagoonal zone, with the relatively elevated amounts of fine grained Zr being transported into the area by stronger winds during the winter or eroded from the watershed during extreme rainfall events. This bed were thus not considered to be a storm deposit. Moreover, the coarser bad at 470–485 cm did not correlated with the obvious peak in the Zr/Rb and Sr/Fe ratios. Consequently, we interpret this coarser grained bed a fluvial flood deposits, with the coarser material transported from the watershed during extreme rainfall events.

The relatively low deposition rate and frequent occurrence of typhoons, mean that it is usually difficult to distinguish every storm event

in coastal lagoon/lake deposits, and storm periods or episodes have been widely used to highlight the variations in millennial-scale storm activity (Donnelly and Woodruff, 2007; Woodruff et al., 2009; Sabatier et al., 2012; Degeai et al., 2015; Adomat and Gischler, 2017). Figs. 8, 9 show that a total of 7 storm periods (SP1 to SP7) occurred over the past 7500 cal yr BP. Our chronostratigraphic model (Fig. 2; Section 5.1) highlights a period of relatively frequent intense typhoon strikes on Hainan Island between 5500 and 3500 cal yr BP, with the exception of one short-lived quieter periods approximately 4100–4900 cal yr BP. Following these relatively active periods is an interval of relatively few extreme coastal flooding events, from 3500 until roughly 1700 cal yr BP, with the exception of one storm period at 2400–2600 cal yr BP. Increased storm activity is again observed between 1700 and −0 cal yr BP (1950 CE), with evidence of two storm periods occurring around 1700–1300 (SP2) and −50 to 1150 cal yr BP (SP1; Figs. 8, 9).

5.3.2. Comparison with historical typhoon record around the South China Sea

We assessed the reliability of our storm record via a comparison with the historical storm records available from the SCS for the past 2000 years (Fig. 8). Chinese historical documents provide a record of past weather and climate phenomena (Liu et al., 2001). The documentary typhoon record of southern China (Hainan Island and Guangdong province) spans at least 1000 years, and the time series of climatic descriptions is almost uninterrupted over the past 500 years (Chen, 1995; Liu et al., 2001). These data have been compiled partly for chapters in various books covering natural disasters or in meteorological records (Qiao and Tang, 1993; Chen, 1995). Fig. S1 shows that the variations of Zr/Rb ratio peaks and percentage of sand (> 63 μm) peaks are consistent with the high frequency period of historical and observational storm records from the eastern Hainan Island. In addition, Fig. 8 shows that the storm periods SP1 evidenced in the XCL-02 sequence also synchronously with Hainan Island and Guangdong province typhoons since around 965 cal yr BP (985 CE), as shown by Chen (1995) and Liu et al. (2001). Furthermore, the SP1 and SP2 phases are closely aligned with the storm coarse fraction events recorded by coral reef lagoon deposits in Xisha Islands over the past 1900 years (Fig. 8; Chen et al., 2012; Wang et al., 2014;Yue et al., 2019). Thus, the significant storm periods SP1–S7 evidenced in the XCL-02 sequence may represent a record of typhoon activity in the northern SCS.

5.4. Tropical cyclone variability and climate change

Previous TC climatology research has focused on linking evidence of millennial-scale TC variability to climate change during the Holocene. The underlying premise of these studies is that changing climatic conditions (e.g. SST, vertical shear of horizontal wind, and the position of high- and low-pressure centers) can change the location and frequency of TC genesis, alter their tracks, vary their intensity, and/or preferentially guide more cyclones into a particular region (Bove et al., 1998; Elsner and Liu, 2003; Liu et al., 2001, 2015; Donnelly and Woodruff, 2007; Woodruff et al., 2009; Lau et al., 2016).

Paleotempestological studies conducted in the northeastern WNP (Japan and Korea) and northern SCS have provided insights into possible linkages between climate change and basin-wide patterns of TC variability. In the northeastern WNP, Woodruff et al. (2009) used sediment coarseness and strontium (Sr) content in lagoonal sediments from Kamikoshiki, Japan, to identify periods of increased TC activity over the past 6400 years. In addition, Yoo et al. (2015) identified 556 storm events in historical records from Korea, covering the period from 1392 to 1910 (Fig. 8). These storm reconstructions from the northeastern WNP suggest significant storm variability over centennial to millennial timescales (Woodruff et al., 2009; Yoo et al., 2015; Katsuki et al., 2017). In the northern SCS, the centennial to millennial-scale storm record from the Xincun lagoon was firstly compared with other storminess proxies in the SCS and WNP. For the past 2000 years, comparisons between the northeastern WNP reconstruction (the Kamikoshiki typhoons and Korean storm records) and storm records from the northern SCS (e.g. the Xincun Lagoon storm sequence, Hainan historical storm records, and Xisha Islands storm events), suggest a roughly inverse relationship (Fig. 8). For example, documentary records of storm episodes in Korea (at 483–553 and 283–323 cal yr BP) were roughly out-of-phase with the storm periods recorded in the Xisha Island lagoon sequence and historical storm records from the Hainan Island and Guangdong province (Fig. 8). This apparently inverse correlation is also evident between TC reconstructions from the northeastern WNP and the Xincun site over the past 7500 years (Fig. 9). For example, high-frequency storm activity recorded in Xincun Lagoon (SP2, SP4, SP5–SP7) generally corresponds with periods of lower storm activity in Kamikoshiki (Fig. 9a, e). In contrast, the quieter conditions in Xincun Lagoon at around 2600–3500 and 4100–4900 cal yr BP are concurrent with periods of increased typhoon-induced overwash events at Kamikoshiki (Fig. 9a, e). The inverse correlation between TC reconstructions from the Xincun Lagoon and northeastern WNP (Korean Peninsula and Japan) may indicate a seesaw pattern in TC activity between the northern SCS and northeastern WNP on the centennial-to-millennial timescales.

Instrumental observations show that ENSO may drive an oscillating pattern in TC activity in the SCS and the WNP (e.g. Chan, 2005; Wang and Chan, 2002; Goh and Chan, 2010). The total number of TCs that develop over the SCS and the WNP is below normal in El Niño years but above normal during La Niña years. However, there is a marked northwestern shift in genesis location during La Niña years and a marked southeastern shift in genesis location during El Niño years (Chan, 1985; Lander, 1994). During La Niña years, typhoons tend to have linear trajectories that may result in a higher likelihood of TC strikes along northern SCS (Elsner and Liu, 2003).

The seesaw pattern in TC activity between the northern SCS and northeastern WNP (Korean Peninsula and Japan) corresponds with observations of modern typhoons, indicating that ENSO droves a seesaw pattern in TC activity in the northeastern WNP (Japan and Korea) and northern SCS over centennial to millennial timescales. To test this relationship between typhoon activity and ENSO during the mid-to-late Holocene in the SCS and the WNP, we compared patterns of typhoon-induced deposition at Hainan Island with an annually resolved El Niño proxy reconstruction from Laguna Pallacocha, Ecuador (Moy et al., 2002). Comparisons between the Hainan Island and Pallcacocha records show a general correlation between periods of increased La Niña occurrence and periods of more typhoon-induced deposition at the study site during the past 7500 cal yr BP (Fig. 9a, f). For example, the typhoon-induced deposits at Xincun of SP3–SP7 are roughly concurrent with periods of increased La Niña activity. In contrast, quieter conditions at Xincun (e.g. 2600–3500 and 4100–4900 cal yr BP) generally occurred during intervals of reduced La Niña activity. Therefore, as with some previous studies that used instrumental and historical observations (Wang and Chan, 2002; Elsner and Liu, 2003), the millennial-scale reconstructions from Xincun support a pattern of increased typhoon strikes in the northern SCS during La Niña years.

However, the trend of storm activity in the northern SCS is not always consistent with ENSO variations (Fig. 9a, f, SP1–SP2). An alternative hypothesis is that storm activity in the Northern SCS is not related solely to ENSO variations at the millennial-scale. It is possible that regional storm activity is also influenced by regional oceanic and atmospheric conditions. Recently, it was hypothesized that the warmer state of the WPWP may be one of the significant factors that impacts on storm activity in the WNP (Ho et al., 2004; Chen and Huang, 2008; Chen et al., 2012; Yue et al., 2019). To examine the role of the thermal state of the WPWP in governing typhoon activity over the mid to late Holocene, we also compared patterns of typhoon-induced deposition at Xincun with the SST deduced from foraminifers retrieved from sediment cores in the WPWP. Comparisons between the Xincun storm sequence and SST records from the WPWP (Fig. 9a, g) show that the

phases of increased storm activity in Xincun lagoon generally occurred during warm episodes. In contrast, the muddy sediments that likely reflect quieter depositional conditions in Xincun Lagoon (e.g. 1700–2400 and 2600–3500 cal yr BP) were typically deposited during colder intervals. This relationship phenomenon agrees with recent meteorological observations (Chen and Huang, 2008). During warm years, the monsoon trough retreats westward and northward so that a low-level cyclonic vorticity anomaly and upper-level divergence anomaly exist in the west quadrant, and this favors TC genesis in the west of the WNP (Chen and Huang, 2008). In contrast, there are more TCs in the southeast of the WNP during cold years. The storm periods correspond well with warmer SSTs in the equatorial western Pacific (Fig. 9), indicating that typhoon pathways were also controlled by the effect of the warm state of the WPWP in the SCS and WNP during the mid-to-late Holocene.

Alternatively, La Niña (El Niño) may strengthen (weaken) the thermal stage of the WPWP and SCS, and so the impact of La Niña (El Niño) is to guide more (less) typhoons towards northern SCS and raise the generate opportunities of local generated typhoons in the SCS (Ho et al., 2004; Wang et al., 2007; Goh and Chan, 2010).

Of note, the stormy period around 3100–3500 cal yr BP in the Xisha Islands is inconsistent with the storm deposition at the study site (Fig. 9a, c), possibly because of the anomalous southerly position of the Intertropical Convergence Zone (ITCZ) over the same period (Haug et al., 2001). A southward shift of the ITCZ potentially leads to an increase in storm genesis in the south of the SCS and the WNP, as well as more storms making landfall in the Xisha Islands, as indicated by Chen et al. (2019). An alternative explanation for this inconsistency is that the stormy period around 3100–3500 cal yr BP may correlate to cooling SST states (Wang et al., 1999; Huang et al., 2009) during El Niño periods (Fig. 9f) in the northern SCS. Local generated TCs in El Nino periods (Fig. 9f) would preferably form in the northern SCS (Goh and Chan, 2010), which caused more storms hit the northern SCS (e.g. Xisha Islands). However, the cooling SST period (3100–3500 cal yr BP) could be unfavourable for TCs movement into the northern part of northern SCS (e.g. Hainan Island) and would greatly inhibite the storm intensity (Wang et al., 2007). And these weakening storms thus would be unlikely to be recorded in the Xincun Lagoon sequence.

6. Conclusion

This study has provided a 7500-yr high-resolution record of past storm events based on a sediment deposits from a coastal lagoon on Hainan Island in the South China Sea. An analysis of the geochemistry and sedimentology of the sediments in the watershed of the lagoon and from the beaches was undertaken to discriminate spatially the source of detrital inputs into the lagoon. Our results reveal that the sedimentary supply from the coastal beaches are characterized by high Zr, Sr, Ca concentrations and very low Fe, Al, Rb, Ti, Mn concentrations. A proxy analysis of the Zr/Rb ratio of the Xincun lagoonal sequence evidences the presence of storm variations during the mid-to-late Holocene.

Our reconstructions from Xincun Lagoon highlighted 7 periods of higher storm frequency during the past 7500 cal yr BP. From a comparison of this reconstruction with the historical records, we found strong coherence between coarse-grained deposits and storm records from the northern SCS. In addition, a comparison with storm proxies from the northern SCS and Northwestern Pacific exhibits an in-phase storminess pattern in the SCS and northeastern WNP. Moreover, a comparison of the Xincun storm record with paleoclimate proxies in the WNP and Eastern Pacific shows that the phases of increased storminess occurred during La Niña periods and warm periods in the WPWP.

Our results further demonstrate the high potential for coastal lagoon settings to record paleostorm events, but also show gaps in our understanding of long-term TC patterns. However, a wider geographical distribution of millennial-scale TC records will be required to study the potential relationships between periods of increased storm activity and other modes of climatic variability such as the Pacific Decadal Oscillation, ITCZ and western Pacific subtropical high.

Acknowledgments

This research was supported by the Natural Science Foundation of China (No. 41706096, 41530962, 41706095, 41771218; 41561064). We wish to thank Jiayu Tu, Baoming Yang, Dandan Wang, Longhui Zhang who helped us in the field work. We especially thank Li Tian at State Key Laboratory of Marine Environmental Science (Xiamen University) for her help with the XRF measurement. Dr. Jinlong Wang of East China Normal University and Dr. Qiang Yao of Indiana State University were appreciated for their kind comments. The author also wishes to thank of Beta laboratory for the AMS^{14}C dating and TL/OSL dating laboratory of Shaanxi Normal University for the OSL dating. Chen Dai help for the seismic profile measurement and Xiaomei Xu participated in grain size analysis.

Appendix A. Supplementary data

Supplementary data to this article can be found online at https://doi.org/10.1016/j.margeo.2019.105987.

References

Adomat, F., Gischler, E., 2017. Assessing the suitability of Holocene environments along the Central Belize coast, Central America, for the reconstruction of hurricane records. Int. J. Earth Sci. 106 (1), 283–309. https://doi.org/10.1007/s00531-016-1319-y.

Baker, R.G.V., Davis, A.M., Aitchison, J.C., Flood, P.G., Morton, B.S., Haworth, R.J., 2003. Comment on “mid-holocene higher sea level indicators from the south china coast” by w.w.-s. yim and g. huang [mar. geol. 182 (2002) 225–230]: a regional perspective. Mar. Geol. 196 (1–2), 91–98. https://doi.org/10.1016/S0025-3227(02)00615-1.

Blaauw, M., Christen, J.A., 2011. Flexible paleoclimate age-depth models using an autoregressive gamma process. Bayesian Anal. 6, 457–474. https://doi.org/10.1214/11-BA618.

Blott, S., 2000. GRADISTAT Version 4.0: a grain size distribution and statistics package for the analysis of unconsolidated sediments by sieving or laser granulometer. URL: http://www.kpal.co.uk/gradistat.abstract.htm.

Boldt, K.V., Lane, P., Woodruff, J.D., Donnelly, J.P., 2010. Calibrating a sedimentary record of overwash from Southeastern New England using modeled historic hurricane surges. Mar. Geol. 275 (1–4), 127–139. https://doi.org/10.1016/j.margeo.2010.05.002.

Boulay, S., Colin, C., Trentesaux, A., Pluquet, F., Bertaux, J., Blamart, D., Buehring, C., Wang, P., 2003. Mineralogy and sedimentology of Pleistocene sediment in the South China Sea (ODP Site 1144). In: Proceedings of the Ocean Drilling Program, Scientific Results. 184 (211). pp. 1–21. https://doi.org/10.2973/odp.proc.sr.184.211.2003.

Bove, M.C., Elsner, J.B., Landsea, C.W., Niu, X., O’Brien, J.J., 1998. Effect of El Niño on US landfalling hurricanes, revisited. B. Am. Meteorol. Soc. 79 (11), 2477–2482. https://doi.org/10.1175/1520-0477(1998)079<2477:EOENOO>2.0.CO;2.

Brandon, C.M., Woodruff, J.D., Lane, D., Donnelly, J.P., 2013. Tropical cyclone wind speed constraints from resultant storm surge deposition: a 2500 year reconstruction of hurricane activity from St. Marks, FL. Geochem. Geophy. Geosy. 14 (8), 2993–3008. https://doi.org/10.1002/ggge.20217.

Camargo, S.J., Sobel, A.H., Barnston, A.G., Emanuel, K.A., 2007. Tropical cyclone genesis potential index in climate models. Tellus A 59 (4), 428–443. https://doi.org/10.1111/j.1600-0870.2007.00238.x.

Cao, X., Li, T., Peng, M., Chen, W., Chen, G., 2014. Effects of monsoon trough intraseasonal oscillation on tropical cyclogenesis over the western North Pacific. J. Atmos. Sci. 71 (12), 4639–4660. https://doi.org/10.1175/JAS-D-13-0407.1.

Chan, J.C., 1985. Tropical cyclone activity in the Northwest Pacific in relation to the El Niño/Southern Oscillation phenomenon. Mon. Weather Rev. 113 (4), 599–606. https://doi.org/10.1175/1520-0493(1985)113<0599:TCAITN>2.0.CO;2.

Chan, J.C., 2005. Interannual and interdecadal variations of tropical cyclone activity over the western North Pacific. Meteorog. Atmos. Phys. 89 (1–4), 143–152. https://doi.org/10.1007/s00703-005-0126-y.

Chen, D.K., Lei, X.T., Wang, W., Wang, G.H., Han, G.J., Zhou, L., 2013. Upper ocean response and feedback mechanisms to typhoon. Adv. Earth Sci. 28 (10), 1077–1086 (in Chinese with English abstract).

Chen, G., Huang, R., 2008. Influence of monsoon over the warm pool on interannual variation on tropical cyclone activity over the western North Pacific. Adv. Atmo. Sci. 25 (2), 319–328. https://doi.org/10.1007/s00376-008-0319-7.

Chen, H., Harff, J., Qiu, Y., Osadczuk, A., Zhang, J., Tomczak, M., Cui, Z., Cai, G., Wen, M., Li, L., 2015. Last glacial cycle and seismic stratigraphic sequences offshore Western Hainan Island, NW South China Sea. In: Clift, P.D., Harff, J., Wu, J., Qiu, Y. (Eds.), River-Dominated Shelf Sediments of East Asian Seas. Geological Society, Special Publications, London, pp. 429. https://doi.org/10.1144/SP429.9.

Chen, H.F., Wen, S.Y., Song, S.R., Yang, T.N., Lee, T.Q., Lin, S.F., Hsu, S.C., Wei, K.Y., Change, P.U., Yu, P.S., 2012. Strengthening of paleo-typhoon and autumn rainfall in

Taiwan corresponding to the Southern Oscillation at late Holocene. J. Quat. Sci. 27 (9), 964–972. https://doi.org/10.1002/jqs.2590.
Chen, H.F., Liu, Y.C., Chiang, C.C., Liu, X.Q., Chou, Y.M., Pan, H.J., 2019. China's historical record when searching for tropical cyclones corresponding to Intertropical Convergence Zone (ITCZ) shifts over the past 2 kyr. Clim. Past 15, 1–11. https://doi.org/10.5194/cp-15-279-2019.
Chen, H.S., 1995. Natural Disasters in Hainan Province during the Past 1000 Years (in Chinese). Hainan Press, Haikou, pp. 1–236 (in Chinese).
Chen, Z., Song, B., Wang, Z., Cai, Y., 2000. Late Quaternary evolution of the sub-aqueous Yangtze Delta, China: sedimentation, stratigraphy, palynology, and deformation. Mar. Geol. 162 (2–4), 423–441. https://doi.org/10.1016/S0025-3227(99)00064-X.
Das, O., Wang, Y., Donoghue, J., Xu, X., Coor, J., Elsner, J., Xu, Y., 2013. Reconstruction of paleostorms and paleoenvironment using geochemical proxies archived in the sediments of two coastal lakes in northwest Florida. Quat. Sci. Rev. 68, 142–153. https://doi.org/10.1016/j.quascirev.2013.02.014.
Degeai, J.P., Devillers, B., Dezileau, L., Oueslati, H., Bony, G., 2015. Major storm periods and climate forcing in the Western Mediterranean during the Late Holocene. Quat. Sci. Rev. 129, 37–56. https://doi.org/10.1016/j.quascirev.2015.10.009.
Dezileau, L., Sabatier, P., Blanchemanche, P., Joly, B., Swingedouw, D., Cassou, C., Castaings, J., Martinez, P., Von Grafenstein, U., 2011. Intense storm activity during the Little Ice Age on the French Mediterranean coast. Palaeogeogr. Palaeoclimatol. Palaeoecol. 299 (1–2), 289–297. https://doi.org/10.1016/j.palaeo.2010.11.009.
Dezileau, L., Perez-Ruzafa, A., Blanchemanche, P., Degeai, J.P., Raji, O., Martinez, P., Marcos, C., Grafenstein, U.V., 2016. Extreme storms during the last 6500 years from lagoonal sedimentary archives in the Mar Menor (SE Spain). Clim. Past 12 (6), 1389–1400. https://doi.org/10.5194/cp-12-1389-2016.
Donnelly, J.P., Woodruff, J.D., 2007. Intense hurricane activity over the past 5,000 years controlled by El Niño and the West African monsoon. Nature 447 (7143), 465. https://doi.org/10.1038/nature05834.
Donnelly, J.P., Roll, S., Wengren, M., Butler, J., Lederer, R., Webb III, T., 2001. Sedimentary evidence of intense hurricane strikes from New Jersey. Geology 29 (7), 615–618. https://doi.org/10.1130/0091-7613(2001)029<0615:SEOIHS>2.0.CO;2.
Donnelly, J.P., Butler, J., Roll, S., Wengren, M., Webb III, T., 2004. A backbarrier overwash record of intense storms from Brigantine, New Jersey. Mar. Geol. 210 (1–4), 107–121. https://doi.org/10.1016/j.margeo.2004.05.005.
Elsner, J.B., Liu, K.B., 2003. Examining the ENSO-typhoon hypothesis. Clim. Res. 25 (1), 43–54. https://doi.org/10.3354/cr025043.
Emanuel, K., 2005. Increasing destructiveness of tropical cyclones over the past 30 years. Nature 436 (7051), 686–688. https://doi.org/10.1038/nature03906.
Folk, R.L., Ward, W.C., 1957. A study in the significance of grain size parameters. J. Sediment. Petrol. 27, 3–26. https://doi.org/10.1306/74D70646-2B21-11D7-8648000102C1865D.
Frappier, A.B., Sahagian, D., Carpenter, S.J., González, L.A., Frappier, B.R., 2007. Stalagmite stable isotope record of recent tropical cyclone events. Geology 35 (2), 111–114. https://doi.org/10.1130/G23145A.1.
Gaertner, M.A., Jacob, D., Gil, V., Domínguez, M., Padorno, E., Sánchez, E., Castro, M., 2007. Tropical cyclones over the Mediterranean Sea in climate change simulations. Geophys. Res. Lett. 34 (14), 176–192. https://doi.org/10.1029/2007GL029977.
Gao, J.H., Chen, G., Ou, W., Zhu, D., 2004. The coast evolution and regulation in Wanquan River estuary, Hainan Island. J. Geogr. Sci. 14 (3), 375–381. https://doi.org/10.1007/BF02837419.
Goh, A.Z.C., Chan, J.C., 2010. Interannual and interdecadal variations of tropical cyclone activity in the South China Sea. Int. J. Climatol. 30 (6), 827–843. https://doi.org/10.1002/joc.1943.
Gong, W.P., Wang, Y.P., Wang, D.R., Mo, L.S., 2008. Hydrodynamics under combined action of wave and tide and its implication for the sediment dynamics in Xincun Tidal Inlet, Hainan. J. Mar. Sci. 26 (2), 1–12 (in Chinese with English abstract).
Grün, R., 2003. Age.Exe. Computer Program for the Calculation of Luminescence Dates. Unpublished Computer Program. RSES, Canberra.
Guilizzoni, P., Marchetto, A., Lami, A., Brauer, A., Vigliotti, L., Musazzi, S., Leonardo Langone, L., Manca, M., Lucchini, F., Calanchi, N., Dinelli, E., 2006. Records of environmental and climatic changes during the late Holocene from Svalbard: palaeolimnology of Kongressvatnet. J. Paleolimnol. 36 (4), 325–351. https://doi.org/10.1007/s10933-006-9002-0.
Haug, G.H., Hughen, K.A., Sigman, D.M., Peterson, L.C., Röhl, U., 2001. Southward migration of the intertropical convergence zone through the Holocene. Science 293 (5533), 1304–1308. https://doi.org/10.1126/science.1059725.
Hayne, M., Chappell, J., 2001. Cyclone frequency during the last 5000 years from Curacoa Island, Queensland. Palaeogeogr, Palaeocl. 168, 201–219. https://doi.org/10.1016/S0031-0182(00)00217-0.
Hennekam, R., de Lange, G., 2012. X-ray fluorescence core scanning of wet marine sediments: methods to improve quality and reproducibility of high–resolution paleoenvironmental records. Limnol. Oceanogr. Methods 10 (12), 991–1003. https://doi.org/10.4319/lom.2012.10.991.
Hippensteel, S.P., 2010. Paleotempestology and the pursuit of the perfect paleostorm proxy. GSA Today 20 (4), 52–53. https://doi.org/10.1130/GSATG80GW.1.
Ho, C.H., Baik, J.J., Kim, J.H., Gong, D.Y., Su, C., 2004. Interdecadal changes in summertime typhoon tracks. J. Clim. 17, 1767–1776. https://doi.org/10.1175/1520-0442(2004)017<1767:ICISTT>2.0.CO;2.
Huang, Y., Jiang, H., Sarnthein, M., Knudsen, K.L., Li, D., 2009. Diatom response to changes in palaeoenvironments of the northern South China Sea during the last 15 000 years. Mar. Micropaleontol. 72 (1–2), 99–109. https://doi.org/10.1016/j.marmicro.2009.04.003.
Jia, J.J., Gao, J.H., Liu, Y.F., Gao, S., Yang, Y., 2012. Environmental changes in Shamei Lagoon, Hainan Island, China: Interactions between natural processes and human activities. J. Asian Earth Sci. 52, 158–168. https://doi.org/10.1016/j.jseaes.2012.03.008.
Jia, J.J., Gao, J., Cai, T., Li, Y., Yang, Y., Wang, Y.P., Xia, X.M., Li, J., Wang, A.J., Gao, S., 2018. Sediment accumulation and retention of the Changjiang (Yangtze River) subaqueous delta and its distal muds over the last century. Mar. Geol. 401, 2–16. https://doi.org/10.1016/j.margeo.2018.04.005.
Jiang, T., Liu, X., Xu, T., Hu, Y., 2018. OSL dating of late Holocene coastal sediments and its implication for sea-level eustacy in Hainan Island, Southern China. Quatern. Int. 468, 24–32. https://doi.org/10.1016/j.quaint.2017.11.039.
Jones, A.F., Macklin, M.G., Brewer, P.A., 2012. A geochemical record of flooding on the upper River Severn, UK, during the last 3750 years. Geomorphology 179, 89–105. https://doi.org/10.1016/j.geomorph.2012.08.003.
Katsuki, K., Yang, D.Y., Seto, K., Yasuhara, M., Takata, H., Otsuka, M., Nakanishi, T., Yoon, Y., Um, I.K., Cheung, R.C.W., Khim, B.K., Kashima, K., 2016. Factors controlling typhoons and storm rain on the Korean Peninsula during the Little Ice Age. J. Paleolimnol. 55 (1), 35–48. https://doi.org/10.1007/s10933-015-9861-3.
Katsuki, K., Yang, D.Y., Lim, J., Lee, J.Y., Asahi, H., Han, M., 2017. Multi–centennial-scale changes in East Asian typhoon frequency during the mid-Holocene. Palaeogeogr, Palaeoclim, Palaeoecol 476, 140–146. https://doi.org/10.1016/j.palaeo.2017.04.004.
Knutson, T.R., McBride, J.L., Chan, J., Emanuel, K., Holland, G., Landsea, C., Held, I., Kossin, J.P., Srivastava, A.K., Sugi, M., 2010. Tropical cyclones and climate change. Nat. Geosci. 3, 157–163. https://doi.org/10.1002/wcc.371.
Krishnaswamy, S., Lal, D., Martin, J.M., Meybeck, M., 1971. Geochronology of lake sediments. Earth. Planet. Sc. Lett. 11, 407–414. https://doi.org/10.1016/0012-821X(71)90202-0.
Lander, M.A., 1994. An exploratory analysis of the relationship between tropical storm formation in the western North Pacific and ENSO. Mon. Weather Rev. 122 (4), 636–651. https://doi.org/10.1175/1520-0493(1994)122<0636:AEAOTR>2.0.CO;2.
Lau, A.A., Terry, J.P., Ziegler, A.D., Switzer, A.D., Lee, Y., Etienne, S., 2016. Understanding the history of extreme wave events in the Tuamotu Archipelago of French Polynesia from large carbonate boulders on Makemo Atoll, with implications for future threats in the central South Pacific. Mar. Geol. 380, 174–190. https://doi.org/10.1016/j.margeo.2016.04.018.
Li, L., Switzer, A.D., Chan, C.H., Wang, Y., Weiss, R., Qiu, Q., 2016. How heterogeneous coseismic slip affects regional probabilistic tsunami hazard assessment: a case study in the South China Sea. J. Geophys. Res. Earth 121 (8), 6250–6272. https://doi.org/10.1002/2016JB013111.
Liang, H.P., Liang, H.Y., Che, Z.W., He, Y.X., Li, L., 2015. A statistical analysis of landfall tropical cyclone in fifty years in Hainan province. Mar. Forecast. 32 (4), 68–74 (in Chinese with English abstract).
Liu, K.B., 2007. Paleotempestology. Encyclopedia of Quaternary Science. Elsevier, Oxford, pp. 1978–1986.
Liu, K.B., Fearn, M.L., 1993. Lake-sediment record of late Holocene hurricane activities from coastal Alabama. Geology 21 (9), 793–796. https://doi.org/10.1130/0091-7613(1993)021<0793:LSROLH>2.3.CO;2.
Liu, K.B., Shen, C., Louie, K.S., 2001. A 1,000-year history of typhoon landfalls in Guangdong, Southern China, reconstructed from Chinese historical documentary records. Ann. Assoc. Am. Geogr. 91 (3), 453–464. https://doi.org/10.1111/0004-5608.00253.
Liu, K.B., McCloskey, T.A., Ortego, S., Maiti, K., 2015. Sedimentary signature of Hurricane Isaac in a Taxodium swamp on the western margin of Lake Pontchartrain, Louisiana, USA. Proc. IAHS. 367, 421–428. https://doi.org/10.5194/piahs-367-421-2015.
Mak, S., Chan, L.S., 2007. Historical tsunamis in South China. Nat. Hazards 43 (1), 147–164. https://doi.org/10.1007/s11069-007-9113-6.
Malmquist, D.L., 1997. Oxygen isotopes in cave stalagmites as a proxy record of past tropical cyclone activity. In: 22nd Conference on Hurricanes and Tropical Meteorology. American Meterological Society, Fort Collins, pp. 393–394.
Mann, M.E., Woodruff, J.D., Donnelly, J.P., Zhang, Z., 2009. Atlantic hurricanes and climate over the past 1,500 years. Nature 460 (7257), 880–883. https://doi.org/10.1038/nature08219.
May, S.M., Vött, A., Brueckner, H., Smedile, A., 2012. The Gyra washover fan in the Lefkada Lagoon, NW Greece—possible evidence of the 365 AD Crete earthquake and tsunami. Earth Planets Space 64 (10), 859–874. https://doi.org/10.5047/eps.2012.03.007.
Mendelsohn, R., Emanuel, K., Chonabayashi, S., Bakkensen, L., 2012. The impact of climate change on global tropical cyclone damage. Nat. Clim. Chang. 2 (3), 205–209. https://doi.org/10.1038/nclimate1357.
Moy, C.M., Seltzer, G.O., Rodbell, D.T., Anderson, D.M., 2002. Variability of El Nino/Southern Oscillation activity at millennial timescales during the Holocene epoch. Nature 420, 162–165. https://doi.org/10.1038/nature01194.
Murray, A.S., Wintle, A.G., 2000. Luminescence dating of quartz using an improved single-aliquot regenerative-dose protocol. Radiat. Meas. 32 (1), 57–73. https://doi.org/10.1016/S1350-4487(99)00253-X.
Nissen, K.M., Leckebusch, G.C., Pinto, J.G., Ulbrich, U., 2014. Mediterranean cyclones and windstorms in a changing climate. Reg. Environ. Chang. 14 (5), 1873–1890. https://doi.org/10.1007/s10113-012-0400-8.
Nott, J., 2004. Palaeotempestology: the study of prehistoric tropical cyclones—a review and implications for hazard assessment. Environ. Int. 30 (3), 433–447. https://doi.org/10.1016/j.envint.2003.09.010.
Nott, J., 2011. A 6000 year tropical cyclone record from Western Australia. Quat. Sci. Rev. 30, 713e722. https://doi.org/10.1016/j.quascirev.2010.12.004.
Nott, J., Hayne, M., 2001. High frequency of "super-cyclones" along the Great Barrier Reef over the past 5000 years. Nature 413, 508–512. https://doi.org/10.1038/35097055.

Olley, J., Caitcheon, G., Murray, A., 1998. The distribution of apparent dose as determined by optically stimulated luminescence in small aliquots of fluvial quartz: implications for dating young sediments. Quat. Sci. Rev. 17 (11), 1033–1040. https://doi.org/10.1016/S0277-3791(97)00090-5.

Pe-Piper, G., Piper, D.J., Wang, Y., Zhang, Y., Trottier, C., Ge, C., Yin, Y., 2016. Quaternary evolution of the rivers of Northeast Hainan Island, China: tracking the history of avulsion from mineralogy and geochemistry of river and delta sands. Sediment. Geol. 333, 84–99. https://doi.org/10.1016/j.sedgeo.2015.12.008.

Qiao, S.X., Tang, W.Y., 1993. Collection and Research of Climate Data from Historical Records in the Guangzhou Area. Guangdong People's Press, Guangdong, China (in Chinese).

Raji, O., Dezileau, L., Von Grafenstein, U., Niazi, S., Snoussi, M., Martinez, P., 2015. Extreme Sea events during the last millennium in the northeast of Morocco. Nat. Hazard. Earth Sys. 15 (2), 2079–2102. https://doi.org/10.5194/nhess-15-203-2015.

Reed, A.J., Mann, M.E., Emanuel, K.A., Lin, N., Horton, B.P., Kemp, A.C., Donnelly, J.P., 2015. Increased threat of tropical cyclones and coastal flooding to New York City during the anthropogenic era. PNAS 112 (41), 12610–12615. https://doi.org/10.1073/pnas.1513127112.

Reimer, P.J., Bard, E., Bayliss, A., Beck, J.W., Blackwell, P.G., Ramsey, C.B., Buck, C.E., Cheng, H., Edwards, R.L., Friedrich, P.M., Grootes, T.P., Guilderson, H., Haflidason, I., Hajdas, C., Hatté, T.J., Heaton, D.L., Hoffmann, A.G., Hogg, K.A., Hughen, K.F., Kaiser, B., Kromer, S.W., Manning, M., Niu, R.W., Reimer, D.A., Richards, E.M., Scott, J.R., Southon, R.A., Staff, C.S.M., Grootes, P.M., 2013. IntCal13 and Marine13 radiocarbon age calibration curves 0–50,000 years cal BP. Radiocarbon 55 (4), 1869–1887. https://doi.org/10.2458/azu_js_rc.55.16947.

Richter, T.O., Van der Gaast, S., Koster, B., Vaars, A., Gieles, R., de Stigter, H.C., Henk, D.H., van Weering, T.C., 2006. The Avaatech XRF Core Scanner: technical description and applications to NE Atlantic sediments. Geol. Soc. Lond., Spec. Publ. 267 (1), 39–50. https://doi.org/10.1144/GSL.SP.2006.267.01.03.

Sabatier, P., Dezileau, L., Condomines, M., Briqueu, L., Colin, C., Bouchette, F., Duff, M.L., Blanchemanche, P., 2008. Reconstruction of paleostorm events in a coastal lagoon (Hérault, South of France). Mar. Geol. 251 (3–4), 224–232. https://doi.org/10.1016/j.margeo.2008.03.001.

Sabatier, P., Dezileau, L., Briqueu, L., Colin, C., Siani, G., 2010. Clay minerals and geochemistry record from Northwest Mediterranean coastal lagoon sequence: Implications for paleostorm reconstruction. Sediment. Geol. 228 (3–4), 205–217. http://doi.org/10.1016/j.sedgeo.2010.04.012.

Sabatier, P., Dezileau, L., Colin, C., Briqueu, L., Bouchette, F., Martinez, P., Siani, G., Raynal, O., Von Grafenstein, U., 2012. 7000 years of paleostorm activity in the NW Mediterranean Sea in response to Holocene climate events. Quat. Res. 77 (1), 1–11. https://doi.org/10.1016/j.yqres.2011.09.002.

Scileppi, E., Donnelly, J.P., 2007. Sedimentary evidence of hurricane strikes in western Long Island, New York. Geochem. Geophy. Geosy. 8 (6), 1–25. https://doi.org/10.1029/2006GC001463.

Sepúlveda, I., Liu, P.L.F., Grigoriu, M., 2019. Probabilistic tsunami hazard assessment in South China Sea with consideration of uncertain earthquake characteristics. J. Geophys. Res-Sol Ea. 124 (1), 658–688. https://doi.org/10.1029/2018JB016620.

Shi, X.J., Yu, K.F., Chen, T.G., Zhang, J.Y., Zhao, J.X., 2007. Progress in researches on sea–level changes in South China Sea since mid-Holocene. Mar. Geol. Quat. Geol. 27 (5), 1–9 (in Chinese with English abstract).

Song, C.J., 1984. Geomorphology and the tidal inlets in the East Coast of Hainan Island. Studia Marine Science of South China Sea (in Chinese) 5, 31–50.

Soria, J.L.A., Switzer, A.D., Villanoy, C.L., Fritz, H.M., Bilgera, P.H.T., Cabrera, O.C., Siringan, F.P., Maria, Y.Y.S., Ramos, R.D., Fernandez, I.Q., 2016. Repeat storm surge disasters of Typhoon Haiyan and its 1897 predecessor in the Philippines. B. Am. Meteorol. Soc. 97, 31–48. https://doi.org/10.1175/BAMS-D-14-00245.1.

Stott, L.D., Cannariato, K.G., Thunell, R., Haug, G.H., Koutavas, A., Lund, S., 2004. Decline of surface temperature and salinity in the western tropical Pacific Ocean in the Holocene epoch. Nature 431, 56–59. https://doi.org/10.1038/nature02903.

Stowasser, M., Wang, Y., Hamilton, K., 2007. Tropical cyclone changes in the western North Pacific in a global warming scenario. J. Clim. 20 (11), 2378–2396. https://doi.org/10.1175/JCLI4126.1.

Sun, Y., Gao, S., Li, J., 2003. Preliminary analysis of grain-size populations with environmentally sensitive terrigenous components in marginal sea setting. Chin. Sci. Bull. 48 (2), 184–187. https://doi.org/10.1360/03tb9038.

Switzer, A.D., Pucillo, K., Haredy, R.A., Jones, B.G., Bryant, E.A., 2005. Sea level, storm, or tsunami: enigmatic sand sheet deposits in a sheltered coastal embayment from southeastern New south Wales. Australia. J. Coastal Res. 21 (4), 655–663. https://doi.org/10.2112/04-0177.1.

The Compile Committee of China Bay Records, 1999. China Bay Records 11th Fascicule (in Chinese). China Ocean Press, Beijing, pp. 109–130.

Toomey, M.R., Donnelly, J.P., Woodruff, J.D., 2013. Reconstructing mid-late Holocene cyclone variability in the Central Pacific using sedimentary records from Tahaa, French Polynesia. Quaternary. Sci. Rev. 77, 181–189. https://doi.org/10.1016/j.quascirev.2013.07.019.

Toomey, M.R., Donnelly, J.P., Tierney, J.E., 2016. South Pacific hydrologic and cyclone variability during the last 3000 years. Paleoceanography 31 (4), 491–504. https://doi.org/10.1016/j.quascirev.2013.07.019.

Wang, B., Chan, J.C., 2002. How strong ENSO events affect tropical storm activity over the western North Pacific. J. Clim. 15 (13), 1643–1658. https://doi.org/10.1175/1520-0442(2002)015<1643:HSEEAT>2.0.CO;2.

Wang, G., Su, J., Ding, Y., Chen, D., 2007. Tropical cyclone genesis over the South China Sea. J. Marine. Syst. 68 (3–4), 318–326. https://doi.org/10.1016/j.jmarsys.2006.12.002.

Wang, H.P., Ji, Y.N., Fu, X.N., Zhao, Z.Z., 2017b. Distribution and Restriction Factors of rare Earth elements in the Sediments from the Mangrove in Dongzhai Harbor, Hainan Island. Trop. Geogr. 37 (1), 82–90 (in Chinese with English abstract).

Wang, J., Du, J., Baskaran, M., Zhang, J., 2016. Mobile mud dynamics in the East China Sea elucidated using ^{210}Pb, ^{137}Cs, ^{7}Be, and ^{234}Th as tracers. J. Geophy. Res–Oceans 121 (1), 224–239. https://doi.org/10.1002/2015JC011300.

Wang, J., Baskaran, M., Hou, X., Du, J., Zhang, J., 2017a. Historical changes in ^{239}Pu and ^{240}Pu sources in sedimentary records in the East China Sea: Implications for provenance and transportation. Earth Planet. Sci. Lett. 466, 32–42. https://doi.org/10.1016/j.epsl.2017.03.005.

Wang, L., Sarnthein, M., Erlenkeuser, H., Grimalt, J., Grootes, P., Heilig, S., Ivanova, E., Kienast, M., Pelejero, C., Pflaumann, U., 1999. East Asian monsoon climate during the Late Pleistocene: high-resolution sediment records from the South China Sea. Mar. Geol. 156 (1–4), 245–284. https://doi.org/10.1016/S0025-3227(98)00182-0.

Wang, L.C., Behling, H., Lee, T.Q., Li, H.C., Huh, C.A., Shiau, L.J., Chang, Y.P., 2014. Late Holocene environmental reconstructions and their implications on flood events, typhoon, and agricultural activities in NE Taiwan. Clim. Past 10 (5), 1857–1869. https://doi.org/10.5194/cp-10-1857-2014.

Wang, M., Zheng, H., Xie, X., Fan, D., Yang, S., Zhao, Q., Wang, K., 2011. A 600-year flood history in the Yangtze River drainage: comparison between a subaqueous delta and historical records. Chin. Sci. Bull. 56 (2), 188–195. https://doi.org/10.1007/s11434-010-4212-2.

Wang, Y., Peter, M.I., Zhu, D., Zhang, Y., Tang, W., 2001. Coastal plain evolution in southern Hainan Island, China. Chin. Sci. Bull. 46 (1), 90–96. https://doi.org/10.1007/BF03187244.

Wang, Z., Xu, H., Zhan, Q., Saito, Y., He, Z., Xie, J., Li, X., Dong, Y., 2010. Lithological and palynological evidence of late Quaternary depositional environments in the subaqueous Yangtze delta, China. Quat. Res. 73 (3), 550–562. https://doi.org/10.1016/j.yqres.2009.11.001.

Wang, Z., Zhuang, C., Saito, Y., Chen, J., Zhan, Q., Wang, X., 2012. Early mid-Holocene Sea-level change and coastal environmental response on the southern Yangtze delta plain, China: implications for the rise of Neolithic culture. Quat. Sci. Rev. 35, 51–62. https://doi.org/10.1016/j.quascirev.2012.01.005.

Wen, K.G., 2007. Disasters in China—Hainan Province (in Chinese). Meteorological Press, Beijing, pp. 1–281.

Woodruff, J.D., Donnelly, J.P., Okusu, A., 2009. Exploring typhoon variability over the mid-to-late Holocene: evidence of extreme coastal flooding from Kamikoshiki, Japan. Quat. Sci. Rev. 28 (17–18), 1774–1785. https://doi.org/10.1016/j.quascirev.2009.02.005.

Woodruff, J.D., Irish, J.L., Camargo, S.J., 2013. Coastal flooding by tropical cyclones and sea-level rise. Nature 504 (7478), 44–52. https://doi.org/10.1038/nature12855.

Xiong, H., Zong, Y., Qian, P., Huang, G., Fu, S., 2018. Holocene Sea-level history of the northern coast of South China Sea. Quaternary. Sci. Rev. 194, 12–26. https://doi.org/10.1016/j.quascirev.2018.06.022.

Yang, D.Y., Han, M., Kim, J.C., Cho, Y.K., Kim, J.Y., Yi, S., Katsuki, K., Williams, H.F., 2017b. Shell and gravel layers caused by storm-induced rip currents during the medieval warm period and Little Ice Age in South Korea. Palaeogeogr. Palaeoclim. Palaeoecol. 487, 204–215. https://doi.org/10.1016/j.palaeo.2017.08.035.

Yang, Y., Gao, S., Zhou, L., Wang, Y., Li, G., Wang, Y.P., Han, Z.C., Jia, P.H., 2017a. Classifying the sedimentary environments of the Xincun Lagoon, Hainan Island, by system cluster and principal component analyses. Acta Oceanol. Sin. 36 (4), 64–71. https://doi.org/10.1007/s13131-016-0939-1.

Yao, Y., Harff, J., Meyer, M., Zhan, W., 2009. Reconstruction of paleocoastlines for the northwestern South China Sea since the last Glacial Maximum. Sci. China. Ser D. 52 (8), 1127–1136. https://doi.org/10.1007/s11430-009-0098-8.

Yao, Y., Zhan, W., Sun, J., Sun, J., 2013. Emerged fossil corals on the coast of northwestern Hainan Island, China: Implications for mid-Holocene sea level change and tectonic uplift. Chinese. Sc. Bull. 58 (23), 2869–2876. https://doi.org/10.1007/s11434-013-5692-7.

Yap, W., Lee, Y., Gouramanis, C., Switzer, A.D., Yu, F., Lau, A.Y.A., Terry, J.P., 2015. A historical typhoon database for the southern and eastern Chinese coastal regions, 1951 to 2012. Ocean. Coast. Manage. 108, 109–115. https://doi.org/10.1016/j.ocecoaman.2014.05.024.

Ye, L., Wang, X., Bao, C.L., 1994. Tsunami the China seas and its warning service. J. Nat. Disa. 3 (1), 100–103 (in Chinese with English abstract).

Yoo, C., Park, M., Kim, H.J., Choi, J., Sin, J., Jun, C., 2015. Classification and evaluation of the documentary-recorded storm events in the Annals of the Choson Dynasty (1392–1910), Korea. J. Hydrol. 520, 387–396. https://doi.org/10.1016/j.jhydrol.2014.11.023.

Yu, K.F., Zhao, J.X., Collerson, K.D., Shi, Q., Chen, T.G., Wang, P.X., Liu, T.S., 2004. Storm cycles in the last millennium recorded in Yongshu Reef, southern South China Sea. Palaeogeogr. Palaeoclim. Palaeoecol. 210 (1), 89–100. https://doi.org/10.1016/j.palaeo.2004.04.002.

Yu, K.F., Zhao, J.X., Shi, Q., Meng, Q.S., 2009a. Reconstruction of storm/tsunami records over the last 4000 years using transported coral blocks and lagoon sediments in the southern South China Sea. Quat. Int. 195 (1–2), 128–137. https://doi.org/10.1016/j.quaint.2008.05.004.

Yu, K.F., Zhao, J.X., Done, T., Chen, T.G., 2009b. Microatoll record for large century-scale sea-level fluctuations in the mid-Holocene. Quat. Res. 71 (3), 354–360. https://doi.org/10.1016/j.yqres.2009.02.003.

Yue, Y., Yu, K., Tao, S., Zhang, H., Liu, G., Wang, N., Jiang, W., Fan, T., Lin, W., Wang, Y., 2019. 3500-year western Pacific storm record warns of additional storm activity in a warming warm pool. Palaeogeogr. Palaeocl. 521, 57–71. https://doi.org/10.1016/j.palaeo.2019.02.009.

Zhang, J.L., Tian, Q.J., Li, F., Gao, Z., Su, G., 2008. Study on neotectonic characteristics and its evolution in northwestern Hainan Island. Earthquake 28 (3), 85–94 (in Chinese with English abstract).

Zhang, Y., Huang, C.C., Pang, J., Zha, X., Zhou, Y., Wang, X., 2015. Holocene palaeoflood

events recorded by slackwater deposits along the middle Beiluohe River valley, middle Yellow River basin, China. Boreas 44 (1), 127–138. https://doi.org/10.1111/bor.12095.

Zhao, H.T., Zhang, Q.M., Song, C., Yuan, J., Qiu, Z., Lin, C., Wen, X., Li, S., Yu, K.F., Xu, C., 1999. Geomorphology and Environment of the South China Coast and South China Sea Islands. Science Press, Beijing, pp. 1–528 (in Chinese).

Zhou, L., Huang, C.C., Zhou, Y.L., Pang, J.L., Zha, X.C., Xu, J., Zhang, Y.Z., Guo, Y.Q., 2016. Late Pleistocene and Holocene extreme hydrological event records from slackwater flood deposits of the Ankang east reach in the upper Hanjiang River valley, China. Boreas 45 (4), 673–687. https://doi.org/10.1111/bor.12181.

Zhou, L., Gao, S., Gao, J., Zhao, Y., Han, Z., Yang, Y., Jia, P.H., 2017. Reconstructing environmental changes of a coastal lagoon with coral reefs in southeastern Hainan Island. Chinese. Geogr. Sci. 27 (3), 402–414. https://doi.org/10.1007/s11769-017-0867-9.

Zhu, W.H., Yang, Y.G., Bi, H., 2004. The concentrations and distribution characteristics of the rare earth elements (REEs) in soils of Hainan Province. Earth. Environ. 32 (2), 20–25 (in Chinese with English abstract).

Zhu, Y.Z., Nie, B.F., Wang, Y.Q., 1991. Coral reef sediments respectively in the southern and northern parts of Nansha Islands. In: Zhao, H.T. (Ed.), Symposium (1) on Geology, Geophysics and Reef Islands of Nansha Islands and Adjacent Areas. Ocean Press, Beijing, pp. 224–232 (in Chinese).

Zong, Y., 2004. Mid-Holocene sea-level highstand along the southeast coast of China. Quat. Int. 117 (1), 55–67. https://doi.org/10.1016/S1040-6182(03)00116-2.

Zonta, R., Botter, M., Cassin, D., Bellucci, L.G., Pini, R., Dominik, J., 2018. Sediment texture and metal contamination in the Venice Lagoon (Italy): a snapshot before the installation of the MOSE system. Estuar. Coastal. Shelf. S. 205, 131–151. https://doi.org/10.1016/j.ecss.2018.03.007.